

Article

Evaluation of the CDOM absorption coefficient in the Arctic seas by Sentinel-3 OLCI data

Dmitry Glukhovets¹, Oleg Kopelevich^{1,*}, Anna Yushmanova^{1,2}, Svetlana Vazyulya¹, Sergey Sheberstov¹, Polina Karalli^{1,2} and Inna Sahling¹

¹ P. P. Shirshov Institute of Oceanology of the Russian Academy of Sciences (SIO RAS), 117997 Moscow, Russia;

² Moscow Institute of Physics and Technology, 141700 Dolgoprudny, Russia

* Correspondence: oleg@ocean.ru; Tel.: +7-916-640-7835

Abstract: The main goal of our work is the revealing of problematic issues related to estimates of the absorption coefficient of colored organic matter in the northern seas from data of the Ocean and Land Color Instrument (OLCI) on the Sentinel-3 satellites. In particular, a comparison of the OLCI standard error estimates ADG443_NN_err., relating to the measurement and retrieval of the geophysical products, with the uncertainties in the real situation of the northern seas, where the natural conditions are extremely unfavorable (first of all, frequent cloudiness, low Sun heights). We conducted a comprehensive multi-sensor study of the uncertainties using various approaches, first at all, directly comparing the data from satellite (OLCI Sentinel-3 and four other ocean color sensors) and field measurements in five sea expeditions 2016-2019, by using the different processing algorithms. Our analysis has shown that the real uncertainties of the final product are significantly higher than the calculated errors of the ADG443_NN_err., which is $\geq 100\%$ and $\sim 10\%$. The main reason for that is the unsatisfactory atmospheric correction. We present the results of the analysis of the different effecting factors (satellite sensors, processing algorithms, use of the other parameters), and formulate the tasks of future work.

Keywords: OLCI Sentinel-3; Barents, Kara seas, absorption coefficient, uncertainties, field data.

1. Introduction

The content of our study is an analysis of problematic issues related to estimates of the absorption coefficient of colored organic matter in the northern seas from data of the Ocean and Land Color Instrument (OLCI) on the Sentinel-3 satellites. Three factors determine the importance of the problem: firstly, a subject of our research - the CDOM absorption coefficient, which is usually the main part of the seawater absorption of solar radiation in the visible range; secondly, the area of our study - the Arctic Basin, the region where global warming is most pronounced; third, OLCI - a new generation of ocean color scanners designed to replace well-known devices such as MERIS and MODIS.

Our possibilities for carrying out such a study are based on a large number of field measurements carried out in the northern seas. in expeditions by the Shirshov Institute of Oceanology Russian Academy of Science (SIO RAS) RV Akademik Mstislav Keldysh in 2016 -2019.

Absorption of solar radiation in the surface layer is one of the factors affecting an increase in water temperature and a decrease in the ice cover area in the Arctic seas, where the global warming is most pronounced (see, for example, [1,2]). The absorption coefficient determines the seawater ability to absorb solar radiation, and the colored organic matter is one of the main absorbing components of seawater (also called *yellow substance* or *gelbstoff*).

Direct determinations of the concentration of CDOM are quite difficult; therefore, its content is usually estimated through the spectral absorption coefficient $ag(\lambda)$, which can be obtained with acceptable accuracy using optical methods, both contact and remote [3,4]. The contribution of the

CDOM absorption must be taken into account when calculating visible solar radiation entering the water column; this is a wavelength range of 400-700 nm, which is of the most important for the ocean primary bioproductivity and called Photosynthetically Available Radiation (PAR); that is also involved in the ocean heat budget [5], determines underwater visibility and use of various equipment for man activity, studying and monitoring of the marine environment.

The colored organic matter plays a role in many biogeochemical processes occurring in the ocean: this fraction is included in the ocean organic carbon cycle [6]; affects the photochemical formation of biologically labile photoproducts [7]; can help to identify the different biogeochemical regimes in the surveyed area [8]; correlates with bacterial activity [9]. CDOM absorption allows one to register the effect of river runoff [10-12], to study the dynamics of water masses [13], to assess water quality [14-16], as well as more accurately estimate the chlorophyll concentration [17].

The conditions for obtaining satellite data in the Arctic Basin are extremely unfavorable, primarily frequent cloud cover, which is an insurmountable obstacle for optical radiation of visible and infrared radiation. Even in conditions of the variable cloudiness, when ocean color data are available in the gaps between the clouds, the data can be distorted by the influence of nearby clouds.

The Ob and Yenisei river runoff brings a large amount of dissolved organic matter into the Kara Sea, which has a significant effect on its bio-optical characteristics [18-21]. The impact of CDOM absorption is most pronounced in the shortwave bands of satellite color scanners, and it can be so high that due to errors in an atmospheric correction, the radiance values of the water column in these spectral channels take negative values. That leads to difficulties in using some algorithms, for example, the Quasi-Analytical Algorithm [22]. For taking into account this feature, a regional SIO RAS algorithm was developed for the Kara Sea [23]. One of the features of this algorithm is that it does not use the remote sensing reflectance values R_{rs} at the shortwave bands (the wavelengths < 488 nm). This algorithm gives good results in the Kara Sea but can be applied to other seas as well. In the Barents Sea, coccolithophore blooms may interfere with standard alg algorithms. These blooms occur in July-September and lead to a significant change in the spectral values of the water-leaving radiance [3,4]. Not all algorithms cope with these changes. The solution to the atmospheric correction problem is beyond the scope of the work, our task is to study the results of its application.

Regional SIO RAS algorithms were derived using the data from SeaWiFS and MODIS color scanners [3,4]. SeaWiFS completed work in December 2010, MODIS-Aqua and MODIS-Terra scanners are still working, even though the duration of their activity (about 20 years already) has far exceeded the planned period of their operation. OLCI color scanners should provide satellite data in the next decade. Sentinel-3 satellite, as part of the European Copernicus program, is primarily an ocean mission. The Sentinel-3A satellite was launched in February 2016 and has been in the routine phase since October 2017. The next Sentinel-3B satellite was launched in April 2018. During the commissioning period, the two satellites have been positioned in tandem configuration, separated by 30 seconds. Once Sentinel-3B is operational, it flies in the same orbit of Sentinel-3A, but 140° ahead. Each satellite carries three main sensors, specifically a SAR radar altimeter, SST radiometer, and ocean and land color instrument (OLCI), revisiting the same place every two days with the two satellites. Next OLCI is supposed to be launched aboard the satellite Sentinel 3C in 2023.

In this article, we highlight a problem of how Sentinel-3 OLCI data may be used with the existing regional algorithms. The absorption coefficient of colored organic matter is included in a list of Essential Climate Variables (ECV) necessary for systematic observations to estimate the climate change in the atmosphere, ocean, and land, according to the program of the Global Climate Observing System (GCOS). The obtained results will be useful for improvement in quality and consistency with applications to inter-annual and climate scale variability. For example, they will be useful for the future issues of the Atlas of the Russian seas bio-optical characteristics [4].

2. Materials and Methods

2.1. Study Area

We analyzed the data of ship measurements performed on five expeditionary cruises of the R/V Akademik Mstislav Keldysh, carried out in 2016-2019. Information on these cruises is presented in

Table 1. In total, we collected 341 stations with in situ measurements of the absorption spectra required for the validation of satellite data. However, due to frequent cloudiness, many of these stations could not be compared with satellite data.

Table 1. Cruises in the Arctic and Atlantic with measured data

Cruise and vessel	Region	Measurement period	Number of stations
AMK-65	Norwegian and Barents Seas	29.06 - 09.07.2016	14
AMK-68	North Atlantic (60-degree section), Barents Sea	30.06 - 7.08 2017	72
AMK-71	North Atlantic (60-degree section), Norwegian and Barents seas	28.06 - 13.08 2018	75
AMK-72	Kara Sea and Laptev Sea	20.08 - 16.09 2018	105
AMK-76	Kara Sea	7.07 - 28.07 2019	47

We focused on the Arctic seas, so for our analysis, we used data only for stations located north of the Arctic Circle; their location is shown in Figure 1. The selection of stations for various types of research is described in Section 3.

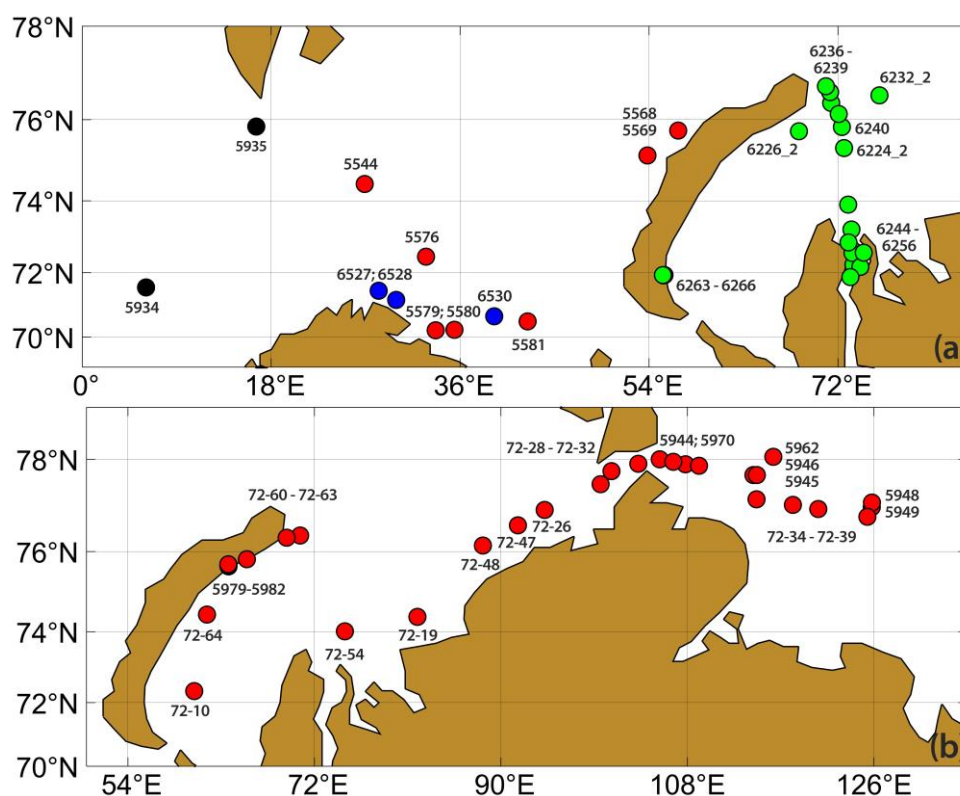
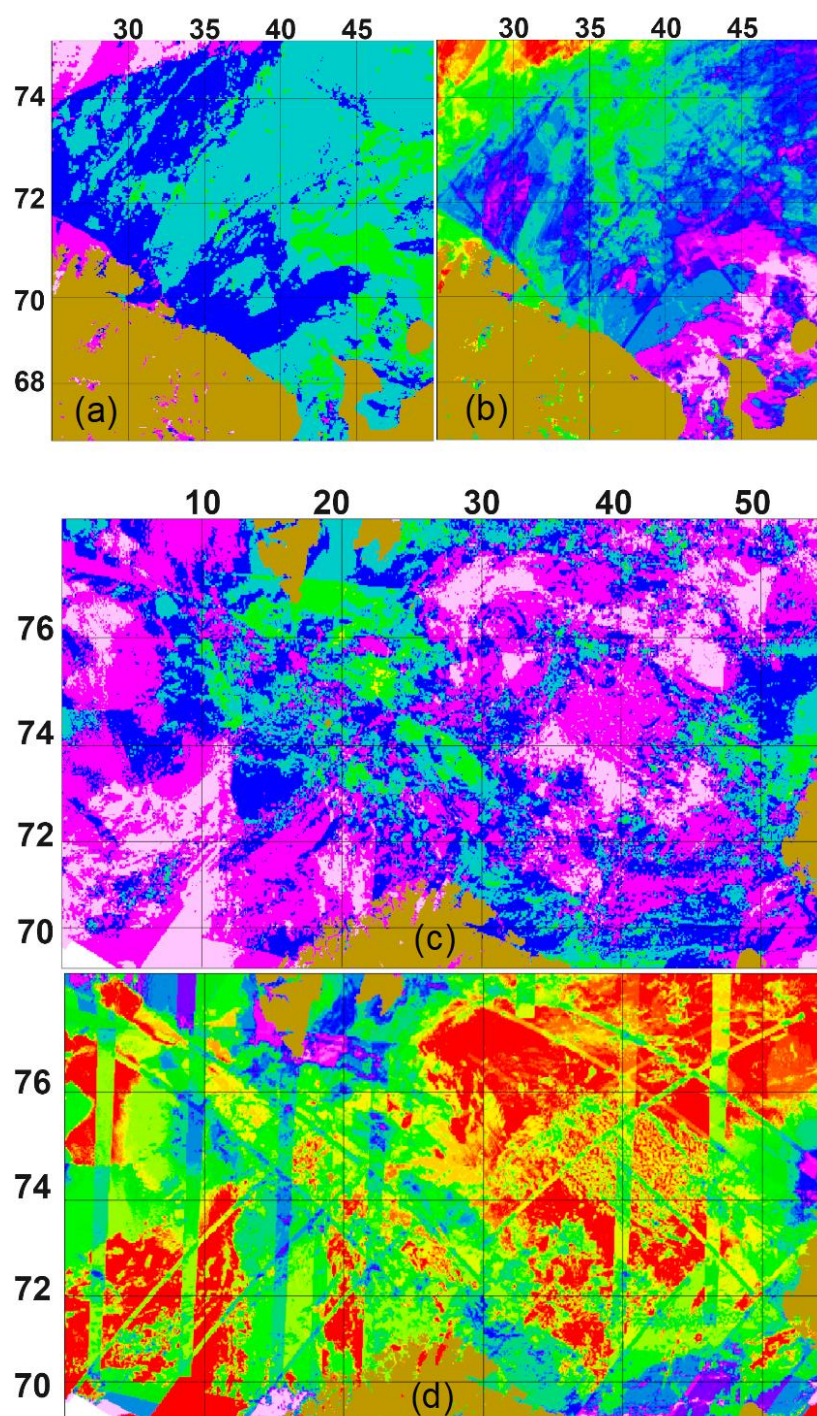


Figure 1. Location of the selected stations: (a) – AMK-65 (blue), AMK-68 (red), AMK-71 (black), AMK-76 (green), (b) – AMK-72.

The weather conditions in the seas under consideration are characterized by almost constant cloud cover; this is an insurmountable obstacle for visible and infrared radiation. Frequent

cloudiness impedes the acquisition of data from simultaneous shipborne and satellite measurements; therefore, the estimation of errors in satellite algorithms is a rather difficult problem for the Arctic seas. Strong horizontal heterogeneity and temporal variability make the error estimation process difficult. Therefore, when using satellite data in the visible range, it becomes necessary to average them over several days or weeks.

Figure 2 shows maps of distributions of the number of days with data for each bin (left) and cloud coverage maps, in accordance with the OLCI_CLOUD flags, averaged over the periods of the voyages. On the cloud coverage maps according to the OLCI_CLOUD flag, the proportion of cloudy days for the averaging period is the greater, the higher the gradation value.



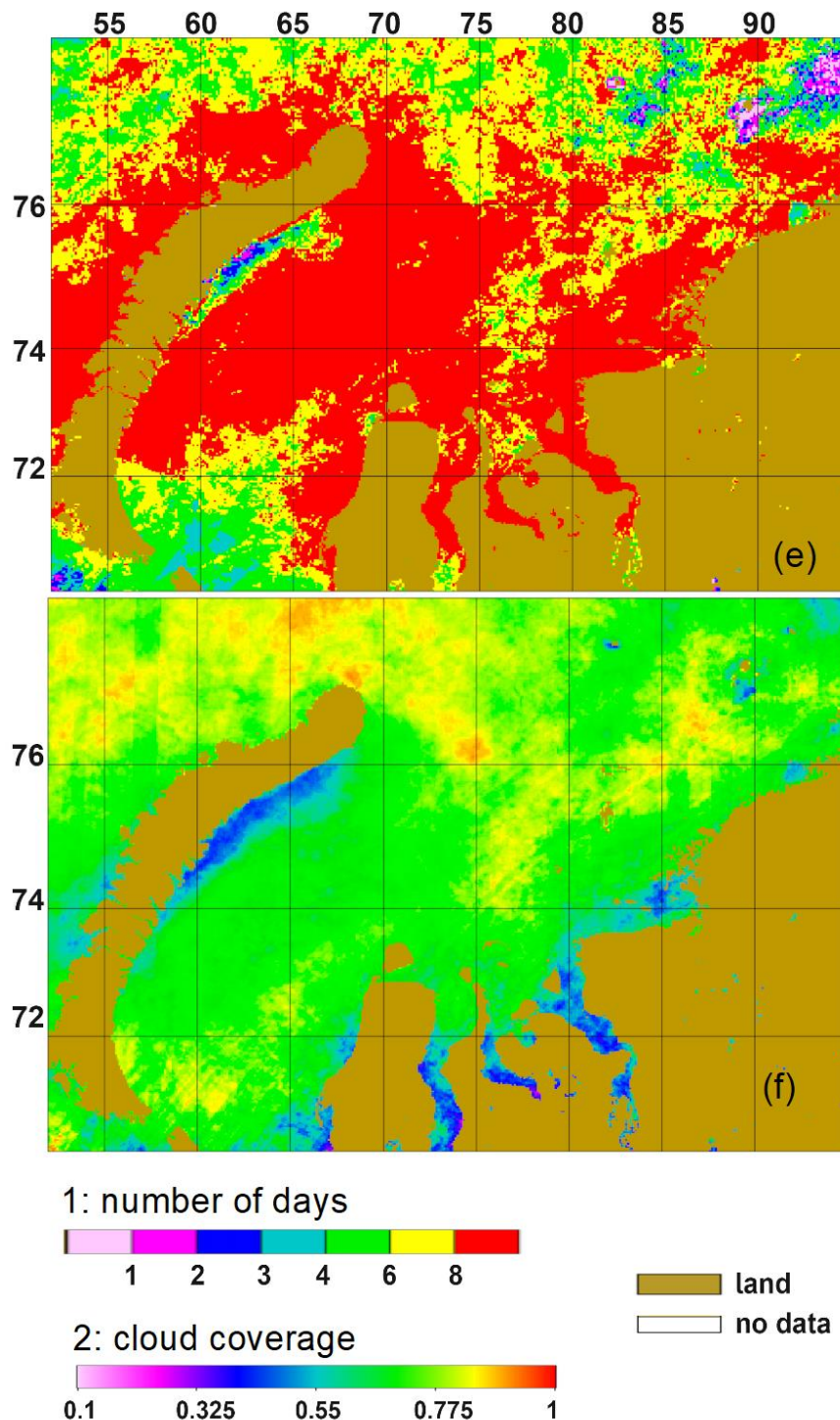


Figure 2. Distributions of the number of days with data per bin (a,c,e; scale 1) and cloud coverage according to OLCI_CLOUD flag data (b,d,f; scale 2). AMK-65: a,b; AMK-68: c,d; AMK-76: e,f.

2.2. Field Measurements

At all selected stations, the absorption coefficients of seawater and its components was determined; at some stations, a floating or a deck spectroradiometer measured the spectral values of the upwelling radiance just beneath the sea surface (a floating device) or the above sea surface (a deck instrument); two irradiance meters BIC and RAMSES (both or one of them) measured the spectral underwater downward and upward irradiances; a transparency meter PUM-A measured the seawater beam attenuation coefficient.

2.2.1 Measurements of the Spectral Absorption Parameters

Spectral seawater absorption coefficients were measured using a portable spectrophotometer in the ICAM (Integrated Cavity Absorption Meter) configuration. ICAM was developed at the Department of Biophysics, Biological Faculty, Moscow State University, Moscow, Russia [24]. Three measured absorption spectra (seawater, filtrate, and empty sphere) for each 330 ml water sample allow us, thanks to using ICAM technology, to eliminate the influence of light scattering.

Knowledge of the effective path length of photons, taking into account their multiple scattering, is necessary to determine the absolute values of the absorption coefficient. Calculations by the Monte Carlo method were carried out, which revealed the absence of dependence of absorption on the scattering properties of seawater. The scattering coefficient in the calculations varied from 0 to 5 m⁻¹ [25].

The CDOM spectra $a_g(\lambda)$ was determined as the difference between the absorption spectral values of the filtrate and pure water [26]. A more detailed description of the measurement and calculation procedure is given in [25,27].

2.2.2 Floating and deck spectroradiometers

For measurements of the spectral upwelling radiance just beneath the sea surface, we used a PRO-1 floating spectroradiometer, developed at the SIO RAS [28]. It also measures the spectral surface irradiance, which makes it possible to calculate the spectral remote sensing reflectance R_{rs} . The measurements are carried out at drift stations, and the device floats off the ship at the distance of 0-50 m to avoid the ship's effects due to shading or reflecting. Depending on weather conditions, 20-50 spectral scans are averaged during processing using a specially developed algorithm. The subsurface radiance reflectance $q(\lambda)$ is calculated as $q(\lambda) = \pi L_u(\lambda)/E_d(\lambda)$, where $L_u(\lambda)$ and $E_d(\lambda)$ are the upwelling radiance and the downwelling irradiance just beneath the sea surface. For continuous monitoring of changes in surface irradiance during measurements, a special DNO sensor is used, installed on an open deck in a place free from shading. The measurements were carried out on the AMK 68th, 72nd, and 76th voyages.

On the AMK-65 and AMK-71 cruises, we used a deck spectroradiometer. It was developed at the Marine Hydrophysical Institute (MHI) [29] to measure the spectral remote sensing reflectance in the range of 390-720 nm with a resolution of 5 nm. This deck spectroradiometer uses a prism monochromator. An optical receiving system is installed on its entrance slit, and the two-beam measurement principle is used with a cosine collector for measuring the sea surface irradiance and a radiance channel lens mounted on opposite ends of the tube. The tube itself is attached in front of the entrance slit of the monochromator.

The ratio of the water radiance and the surface irradiance is measured; the calibration was performed against the reference screen. The measurement is taken from the ship at a 45° zenith angle and the azimuthal angles where the sun's glints were minimal. After measuring the sea surface radiance reflectance, the spectrophotometer measures the radiance reflectance the cuvette with absorbing walls and bottom, filled with water. If the measurements are carried out under the same conditions, the use of a cuvette makes it possible to take into account the reflected component. The averaging several sequential measured values allow us to eliminate random errors.

2.2.3 Measurements of the diffuse attenuation coefficient K_d

To calculate the diffuse attenuation coefficient, we used data on underwater spectral irradiance $E_d(z, \lambda)$, measured by two irradiance meter BIC and RAMSES.

A spectral underwater irradiation meter RAMSES ACC-VIS (TRIOS, Germany) has 190 spectral channels in the spectral range of 320–950 nm (spectral resolution is 3 nm) and accuracy of ±5%. To conduct measurements in the sounding mode, we used a special protective frame, and the data was transmitted to the ship laboratory by a cable. TRIOS provided calibration of the instrument to the National Institute of Standard and Technology (NIST) standards.

The other irradiance meter, E-meter (BIC 2100), has two measuring modules for the surface and underwater irradiance; both simultaneously measure the irradiance in four spectral bands 443, 490, 555, and 625 nm. The specialists from SIO RAS modernized the device to perform measurements in an autonomous regime, without a cable. We calibrated the instrument at the SIO RAS before each expedition, according to the working standard of the spectral irradiance density.

The measured $E_d(z, \lambda)$ values allow us to compute the diffuse attenuation coefficients $K_d(\lambda)$ for underwater irradiance, assuming the exponential law $E_d(z) = E_d(0^-) \exp[-K_d z]$, where wavelength λ is omitted for simplicity. In this work, we used $K_d(\lambda)$ values for the upper uniform layer whose thickness is varied from 10 to 30 m.

The maximum depth Z^* , which is available for satellite observations, is assumed equal to the depth for which the contribution of the radiance coming from depths greater than Z^* is less than 10% of the total radiance. Then $Z^* = 1.15/K_d$. According to our field measurements, the $K_d(490)$ varied from 0.03 to 0.34 m^{-1} for the North Atlantic and the Barents Sea and within 0.06-0.36 m^{-1} for the Kara Sea. Hence the informative satellite depth Z^* was within 3.2-18.5 m in the Kara Sea and 3.4-38 m in the Norwegian and Barents Seas. Usually, the thickness of the layer, where the K_d calculations were carried more than the Z^* value. Only in the clear waters of the Barents Sea (stations 5557, 5560, AMK-68), the Z^* value was more than the depth of the layer for field measurements.

2.2.4 The beam attenuation coefficient measurements

These measurements are used for comparison with the backscattering coefficient values b_{bp} calculated from R_{rs} values measured with floating/deck spectroradiometers and satellite color scanners (see Section 3.3). The measurements were carried out using a PUM-A transparency meter in the laboratory mode - on water samples or as part of a ship's flow system.

PUM-A technical characteristics:

- Attenuation coefficient measurement range 0.050 – 1.0 m^{-1} ;
- Measurement error of the attenuation coefficient – 0.005 m^{-1} ;
- Wavelength of attenuation measurement – 530 nm;
- Half-width of the spectral range – 25 nm;
- The amount of internal non-volatile memory – 2 GB;
- Autonomy (time of continuous work)– 5 hours;
- Volume of the measuring cuvette PUM-A – 270 mL.

For control of the stability of measurements, the cuvette was filled with ultrapure type 1 water prepared at the Institute of Oceanology of the Russian Academy of Sciences, following ASTM, CAP, and NCCLS standards on a "Simplicity 185" apparatus by "Millipore." The measured values of the attenuation coefficient were $c = 0.057 \text{ m}^{-1}$. The control of the PUM is also carried by the inter-calibration of the PUM-A device with a submersible PUM transparency meter; the beam attenuation coefficient values of the water sample from the bottle, measured by PUM-A in a cuvette, were compared with the PUM data on the same horizon. The difference did not exceed 0.01 m^{-1} .

2.3. Satellite data and algorithms

2.3.1. Satellite data and software

We ordered the data of the first and second levels of the OLCI-A and OLCI-B sensors at <https://archive.eumetsat.int/usc/>, and the data MODIS-Aqua, VIIRS NPP and VIIRS NOAA - on the website <https://oceancolor.gsfc.nasa.gov/>.

Level 2 satellite data were processed using software developed by the Ocean Optics Laboratory of Shirshov Institute of Oceanology [30], designed to batch process large datasets of ocean color scanners. The set of programs includes the modules for calculating new products and recording results in HDF and/or NetCDF format, averaging data, exporting maps in a given projection, matching in situ and satellite observations, etc. The essential feature of this software is the dynamic loading of libraries that can be developed and implemented by users without having to recompile programs. For the convenience of using programs designed for working with data in the NASA

format developed by the Ocean Biology Processing Group (OBPG) at NASA's Goddard Space Flight Center, we prepared a converter transforming OLCI data to the above-mentioned SeaWiFS-like format and applied this software for converting the OLCI level 2 data. The following standard products were used: OLCI water-leaving reflectance (16 bands), absorption coefficient, Total Suspended Matter (TSM) concentration, and the diffuse attenuation coefficient K_d . When processing, the following data flags were used: OLCI_LAND, OLCI_CLOUD, LCI_CLOUD_AMBIGUOUS, OLCI_CLOUD_MARGIN. For maps building, we binned the data on a 3 by 3 km grid.

The software [30] allows us to process the Level 2 data from MODIS-Aqua, VIIRS SNP, and VIIRS NOAA sensors. These data include the remote sensing reflectance R_{rs} as well as the diffuse attenuation coefficients $K_d(490)$. Using the values of the R_{rs} , the absorption coefficients of yellow substance a_g and the particle backscattering coefficients [4] were calculated for the field stations where a time difference between satellite and field measurements was no more 24 hours. Since the algorithms for these products were developed for MODIS color scanners, we interpolated the VIIRS R_{rs} to MODIS wavelengths. When calculating the parameters, the pixels flagged with LAND, CLDICE, SEAICE or STRAYLIGHT were used.

The software Sentinel Application Platform (SNAP), developed by Brockmann Consult, allows us to work with the OLCI Level 1 data and derive the water-leaving radiance from the TOA (Top Of Atmosphere) radiances. The neural network processor C2RCC (Case 2 Regional Coast Colour), developed by Doerffer and Schiller [31], provides us the opportunity to derive the seawater inherent optical properties, including the seawater absorption of detritus and yellow substance as well as the particle backscattering coefficient.

2.3.2. Algorithms

For calculating the IOP from remote sensing data, primarily for calculating the absorption coefficients, and also the backscattering coefficient b_b and the TSM concentration, we used the algorithms listed below.

OLCI NN

The standard product ADG443_NN (colored Detrital and Dissolved Material absorption coefficient) is obtained in OLCI Level 2 files, as a result of the operation of IMT (Inverse Modeling Technique) neural networks. The spectral remote sensing reflectance R_{rs} is obtained to the input after standard or neural network atmospheric correction.

The SNAP program, developed by ESA (The European Space Agency), as a result of the operation of the C2RCC neural network processor, can also provide other IOPs data.

GIOP

A model of the optical properties of seawater - GIOP (Generalized Inherent Optical Property) was presented in [33,34]. The algorithm is based on the application of various analytical models, parameterized for the surface layer in different seasons. The algorithm uses $R_{rs}(\lambda)$ in the visible range and can derive the absorption coefficients of the colored dissolved organic matter ($a_g(\lambda)$) and of phytoplankton pigments ($a_{ph}(\lambda)$), as well as the particle backscattering coefficient $b_{bp}(\lambda)$. Based on the obtained data on the remote sensing reflectance $R_{rs}(\lambda)$, the model performs an inversion to find the optimal set of the bio-optical characteristics of the water column, which minimizes the difference between the simulated and the measured values. The model provides for the possibility of adjusting input parameters (such as chlorophyll concentration, the spectral slope for the yellow substance absorption).

The Quasi-Analytical Algorithm (QAA)

This algorithm was evolved by Lee et al. [22] to determine the backscattering and absorption coefficients from the spectral remote-sensing reflectance $R_{rs}(\lambda)$, as a result of analysis of several empirical, analytical and semi-analytical models, in particular, Gordon et al. [35], Lee et al. [36]. The spectral $b_b(\lambda)$ is presented by the generally utilized expression [37,38].

Along with the $b_b(\lambda)$, the QAA algorithm can derive the seawater absorption coefficient and make estimates of the values of the detrit-gelbstoff and the phytoplankton pigment absorption

coefficients. The European Space Agency (ESA) Ocean Colour (OC) Climate Change Initiative (CCI) selected the QAA algorithm to derive b_{bp} for creating a long-term series of satellite ocean color products.

Regional semi-analytical algorithm (RSA)

The regional semi-analytical algorithm was developed to estimate the yellow substance absorption coefficient a_g , particle backscattering coefficient b_{bp} , and diffuse attenuation coefficient $K_d(\lambda)$ at four spectral channels 443, 490, 555, and 625 nm in the Kara and White Seas using MODIS satellite data [23]. It uses the R_{rs} data for the wavelength range ≥ 488 nm; the above-surface remote-sensing reflectances $R_{rs}(412)$ and $R_{rs}(443)$ are not used, as the probability of atmospheric correction errors for them is very high. The inverse problem of finding seawater absorption $a(\lambda)$ and backscattering $b_b(\lambda)$ is solved using low-parametric models in which these seawater coefficients are represented as a superposition of the contributions of the main components. The absorption coefficient $a(\lambda)$ is defined as the sum of the absorption of pure sea water, yellow substance or CDOM, and the phytoplankton pigments, while $b_b(\lambda)$ is defined as the superposition of the backscattering by pure sea water and the suspended particles. The contribution of chlorophyll is accounted for by using a regional algorithm for the Kara Sea [39]. An iterative approach was used to improve the accuracy when estimating the slope of the absorption spectrum. As a result of solving the inverse problem, two parameters are defined: $a_g(443)$ and $b_{bp}(555)$, these parameters also allow calculating the $K_d(\lambda)$ value by using a Gordon's formula [40]. The development and validation of the RSA algorithm was performed with the shipboard measurement data, which contain no errors from atmospheric correction; the algorithm was also tested on satellite data and showed acceptable results [23]. In the regional algorithm [39], the chlorophyll concentration is calculated with the formula $\ln(\text{Chl}) = -6.64 \ln[R_{rs}(531)/R_{rs}(547)] - 0.265$. This formula was derived based on the satellite data for R_{rs} and in situ measurements of the chlorophyll concentrations in the Kara Sea in 2007, 2011 and 2013-2015. In the present work, the RSA algorithm was modified to the OLCI spectral channels and now it uses the R_{rs} data for the wavelength range greater or equal 490 nm.

Algorithm for determining b_{bp} and TSM.

The algorithm [41] was developed for cases where the semi-analytical algorithm cannot work properly due to large errors in atmospheric correction; this situation is typical in the Barents and White Seas. The simplified algorithm uses only two wavelengths SeaWiFS 510 and 555 nm, where the errors in atmospheric correction are much less than at 412, 443 and 490 nm. To obtain the particle backscattering coefficient $b_{bp} = b_{bp}(555)$, the diffuse attenuation coefficient $K_d(555)$ and the parameter $X(555)$ are calculated, where $X(555) = b_b(555) / [a(555) + b_b(555)]$, $a(555)$ and $b_b(555)$ are the seawater absorption and backscattering coefficients. The value of $X(555)$ is determined through the value of the normalized water-leaving radiances $L_{wn}(555)$, and $K_d(555)$ through the ratio $L_{wn}(510) / L_{wn}(555)$. The value $[a(555) + b_b(555)]$ can be obtained from $K_d(555)$ using the standard formula [40]. The backscatter b_{bp} is calculated as the difference between the b_b of seawater and the known backscatter b_{bw} of pure water.

The TSM concentration from satellite data is calculated using a regional algorithm obtained on the basis of ship measurements on cruises 13 and 14 of the R/V Akademik Sergey Vavilov (August-September 1998). The data on quasi-simultaneous measurements of the upwelling radiance L_{wn} (floating spectroradiometer) and TSM were used. First, the b_{bp} values were obtained, and then the regression equation TSM vs. b_{bp} was derived: $\text{TSM} = 73.5 b_{bp} + 0.016$, where b_{bp} is measured in m^{-1} and TSM is in mg/L . The average error in determining the concentration of suspended matter is about 30%.

3. Results

This section presents the results of comparing the absorption values of the colored organic matter ADG_443, available on the OLCI website as a standard product ADG_443_NN of the 2nd level, with the data of direct measurements of the absorption coefficient by the ICAM device (section

2.2). For control, we also calculated the ADG_443 values using the SNAP program C2RCC processor [32].

Errors in estimating bio-optical parameters from satellite data are due to various factors, in particular, errors in an atmospheric correction, connected with bad observation conditions and errors of the algorithms used. In the Arctic seas, significant losses in satellite data occur due to cloudiness, a frequent phenomenon in this region. It was cloudiness that did not allow obtaining a full amount of data for the above comparison, even thorough a large number of field measurements was obtained in five voyages of the R/V «Akademik Mstislav Keldysh» in 2016-2019, It is worth to note a principal difference between the field data and satellite measurements: the former were obtained at a point, the latter for a sufficiently large area (the size of such an area (pixel) for OLCI data with a full spatial resolution of WFR is 0.3 km).

In our work, we try to compensate for the lack of a sufficient amount of data to obtain reliable statistical estimates by the complexity of the comparison. For that, we used data from other field measurements to confirm the results obtained. These data included the remote sensing reflectance $R_{rs}(\lambda)$ measured by floating or deck spectroradiometers, the spectral diffuse attenuation coefficient of the underwater irradiance $K_d(\lambda)$, the beam attenuation coefficient c , as well as data from other satellite color scanners, results of calculations by various algorithms (see Section 2.2-2.3).

3.1. Validation and analysis of the ADG_443 values derived from OLCI data

The absorption coefficient of the colored organic matter ADG_NN (starting now ag_olci_std) is available as a standard product of the 2nd level of the OLCI instrument on the Sentinel 3A, B satellites (see Section 2.2). Results of comparing ag_olci_std with the data of direct measurements of the absorption ICAM (ag_icam) are shown in Figure 3.

Figure 3.a shows the complete dataset (151 points), including the estuaries of the Ob and Yenisei rivers (stations 6244-6256 and 72-54, 72-19 in Figure 1 (map)); Fig. 3.b (89 points) excludes river mouths, as well as stations with large zenith angles of the sun (more than 75°) and other factors that impede obtaining quality data (see Section 3.2).

Even after excluding the above stations, as we see in Figure 3.b, the scatter of points is enormous, especially for the Kara Sea, where the difference between the OLCI_ADG_443_standard values for the same ag value according to ICAM data can be more than 30 times. The main reason for such discrepancy is the errors of atmospheric correction since the results for the absorption values calculated from the R_{rs} data measured by the floating (deck) spectroradiometer are incomparably better (see below).

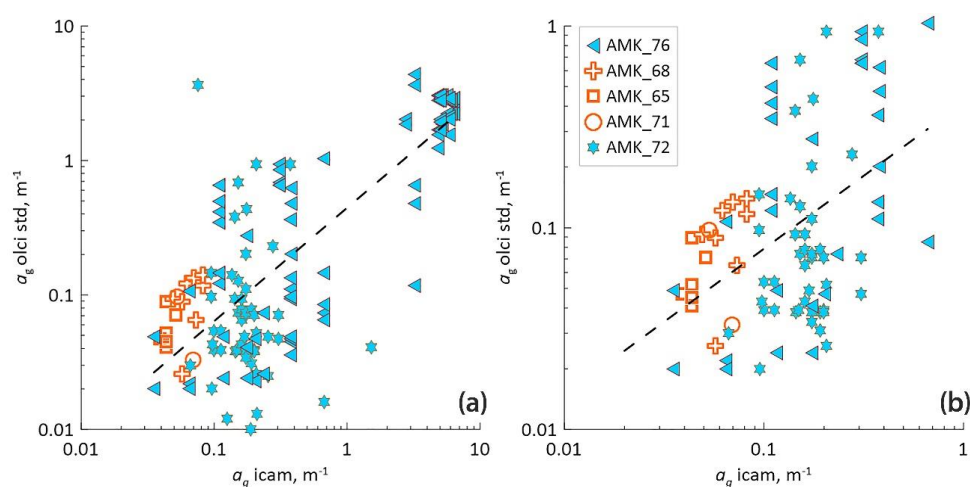


Figure 3. (a) - complete dataset; 3.1 (b) - river estuaries excluded. The Barents Sea is orange, the Kara and Laptev Seas is turquoise. Various cruises are represented by symbols. The dotted line is the correlation across all data.

An analysis of atmospheric correction errors given in Section 3.2 allows us to select 15 stations with acceptable atmospheric correction. Station 6240 in the Kara Sea was excluded due to the strong spatial variability around this station (see Section 3.2), and station 5704 as located south the polar front. Below, we have 13 selected stations, however, for some of them, several passes of Sentinel 3A, B satellites are acceptable, and the total number of OLCI data used was 19 (10 for the Barents Sea, 9 for the Kara Sea).

Figure 4 shows the results of comparing the absorption values calculated from the R_{rs} measurements by the floating (deck) spectroradiometer using different algorithms with the values measured by the ICAM device at the 13 aforementioned stations.

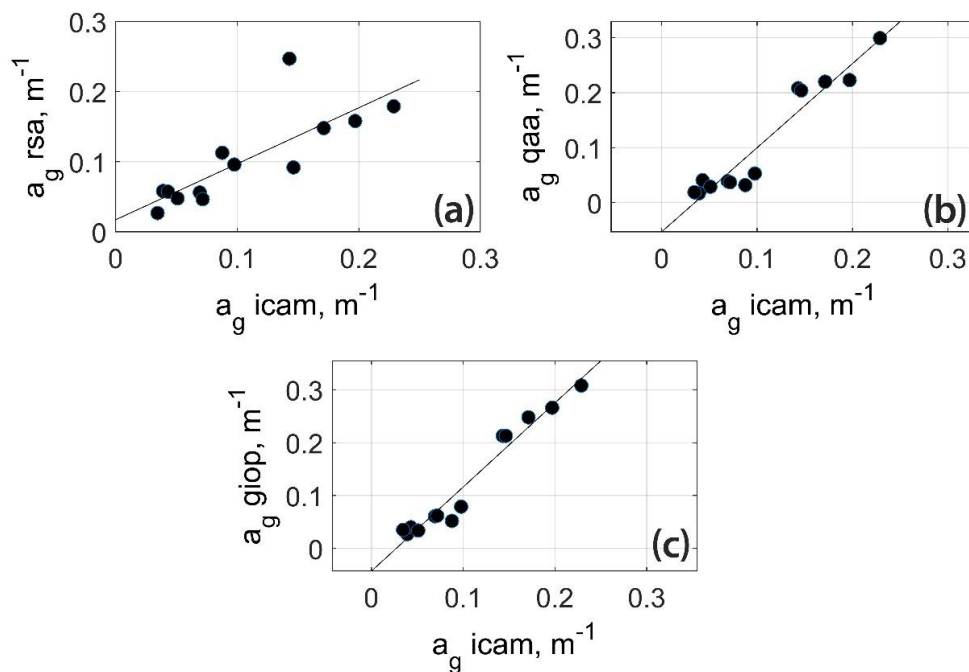


Figure 4. Comparison of the absorption values calculated from the R_{rs} measurements by the floating (deck) spectroradiometer using different algorithms with the values measured by the ICAM device for 13 stations. Solid line - correlation across all data. (a)- RSA algorithm; (b) QAA; (c) - GIOP (see section 2.3).

The values of the determination coefficients R^2 turned out to be large enough for all the algorithms used: 0.656 for RSA, 0.922 for QAA, 0.960 for GIOP.

The calculation of the absorption coefficients from satellite data was also carried out for four other satellite sensors - MODIS-Aqua, MODIS-Terra; VIIRS SNPP, and VIIRS NOAA-20) using the above algorithms. Along with the standard ADG_443_NN values, the ag_OLCI_C2RCC values were calculated using the L1 level OLCI data by the C2RCC processor of the SNAP program [32]. All algorithms, except for neural networks, gave negative values in the calculations for individual flyby; that caused the difference in the number of data pairs (Table 2) The atmospheric correction errors are described in more detail in Section 3.2.

Figure 5 shows the regressions of the calculated values of ag_olci_std and ag_OLCI_C2RCC versus the measured values of ag_icam ; the regression parameters are presented in Table 3.

As can be seen from the Table 3, for the Barents Sea OLCI standard product, a quite acceptable correlation is obtained; the relationship for the Kara Sea is insignificant. For the ag_OLCI_C2RCC values, a significant relationship is observed for both seas, and this relationship is even closer for the Kara Sea than for the Barents Sea.

Table 2. Regression parameters between satellite data and in situ for various algorithms and neural networks (NN) OLCI. N is the number of pairs for calculating the regression, R2 is the coefficient of determination.

	MODIS				VIIRS				OLCI			
	Aqua		Terra		SNPP		NOAA-20		Standard		C2RCC	
	N	R2	N	R2	N	R2	N	R2	N	R2	N	R2
RSA	21	0.52	23	0.44	23	0.38	12	0.29	18	0.04	14	0.24
QAA	21	0.27	15	0.03	20	0.55	8	0.13	18	0	19	0.47
GIOP	24	0.02	30	0.2	30	0.08	13	0.02	19	0.08	19	0.33
NN									19	0.04	19	0.03

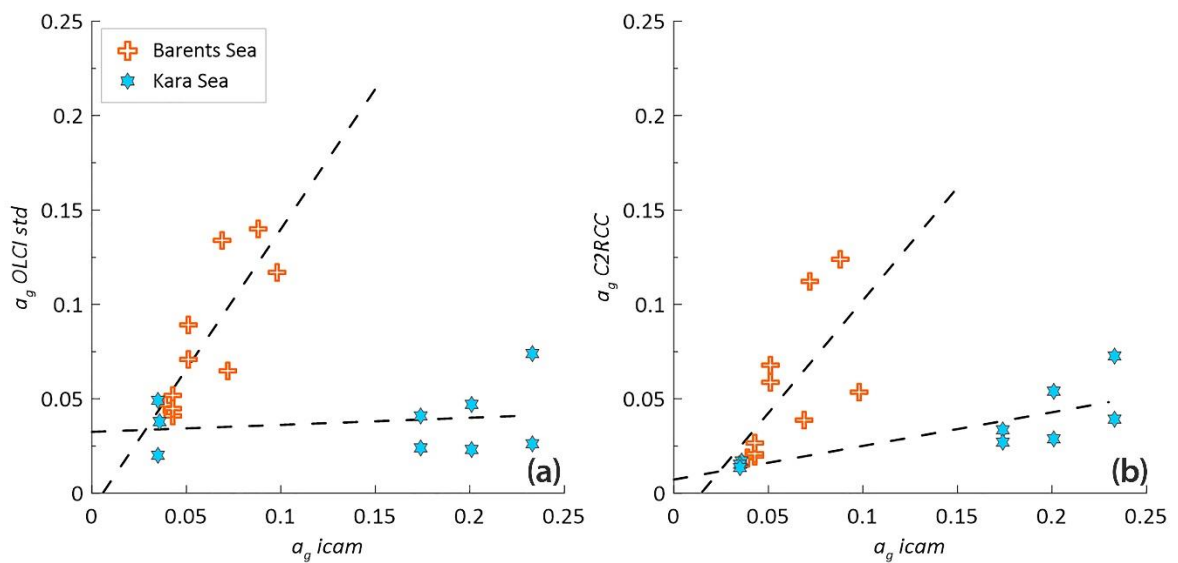


Figure 5. Regressions of satellite values $a_{g_olci_std}$ (a) and $a_{g_OLCI_C2RCC}$ (b) versus measured values a_{g_icam} . The dotted lines represent the correlations for the corresponding seas.

Table 3. Regression parameters of absorbance values calculated from OLCI data ($a_{g_olci_std}$ (a) and $a_{g_OLCI_C2RCC}$ (b)) versus those measured by ICAM (a_{g_icam}). RE - relative error.

Sea	n	Regression equation	$\langle X \rangle$	$\langle Y \rangle$	R2	s_regr.	RE,%
OLCI_standard vs. ag_ICAM							
Barents	10	$Y = 1.48 X - 0.008$	0.06	0.08	0.670	0.023	28
Kara	9	$Y = 0.037 X + 0.032$	0.147	0.038	0.035	insignificant	-
OLCI_C2RCC vs. ag_ICAM							
Barents	10	$Y = 1.19 X - 0.017$	0.06	0.054	0.430	0.03	56
Kara	9	$Y = 0.178 X + 0.007$	0.147	0.033	0.624	0.012	38

We want to derive the correcting equations, allowing us to obtain the satellite absorption coefficient values closer corresponding to the measured values. For that, it is necessary to calculate the inverse regression equations a_{g_corr} vs. $a_{g_olci_std}$ or a_{g_corr} vs. a_{g_C2RCC} . The results of this calculation are presented in Table 4. Unfortunately, for the Kara Sea, the correction equation for $a_{g_OLCI_standard}$ is impossible due to the insignificance of the correlation. Still, it is possible for the absorption coefficient values calculated with the C2RCC processor.

Table 4. Correction equations for calculating absorbance values according to OLCI data that better correspond to direct measurements.

Sea	n	Regression equation	<X>	<Y>	R2	s_regr.	RE,%
ag_corr vs. OLCI_standard							
Barents	10	$Y = 0.67 X + 0.020$	0.06	0.06	0.670	0.030	55
ag_corr vs. OLCI_C2RCC							
Barents	10	$Y = 0.43 X + 0.034$	0.06	0.06	0.430	0.011	18
Kara	9	$Y = 0.62 X + 0.055$	0.147	0.147	0.624	0.045	30

Applying the C2RCC processor, as can be seen from Table 4, the coefficient of determination for the Kara Sea turns out to be even higher than for the Barents Sea, and the regression errors are also quite acceptable. As noted above, the statistical support of the obtained equations is insufficient, and it is too early to recommend them for practical use. In Section 3.4, we will test the obtained equations with the diffuse attenuation coefficient values.

At the end of this section, we will give an example of correcting the a_g spatial distributions using the derived equation for the Barents Sea. Figure 6 shows the ADG_443 spatial distributions in the Barents and partly in the Norwegian Seas built with standard $ag_OLCI_standard$ and corrected ag_corr data for AMK-65 and AMK-68 cruises. Adjusted distributions look more plausible; a vast white area between 30 and 50 deg. d. in Figure 6B due to a lack of satellite data due to cloudiness.

3.2 Results of atmospheric correction

As shown in the previous section, the quality of the atmospheric correction is critical for obtaining reliable absorption coefficient values. Unfortunately, in the conditions of the Arctic seas, ensuring an acceptable quality of atmospheric correction is a most challenging task due to extremely unfavorable natural conditions: it is often cloudy, which leads to a significant loss of data; low angles of the Sun. In this section, we estimate the atmospheric correction errors as a function of various factors, using Rrs as a reference to compare the values of the spectral radiance reflectance directly above the sea surface.

We selected 189 data pairs based on the requirement that a time difference between the in situ measurement and the satellite overpass is not exceeding 24 hours. Figure 7 shows the dependencies of the standard error RMSE of Rrs on the difference between the time of the in situ measurement and the satellite overpass (Figure 7A) and on the solar zenith angle (Figure 7B).

Both figures show a large scatter of points. As seen, a weak trend is observed in both cases - the errors increase with increasing the time difference between the field and satellite measurements and the solar zenith angle. Still, one can see the RMSE values of about 0.001 even though with a time difference of more than 20 hours and the solar zenith angles more 70°. Conversely, the errors exceeding 0.004 can be detected with a time difference of fewer than 5 hours and angles less than 50°. Next, we will consider the influence of various factors in more detail, and we will start with the errors of atmospheric correction associated not with the atmosphere and observation conditions, but with the optical characteristics and processes occurring in the surface water layer.

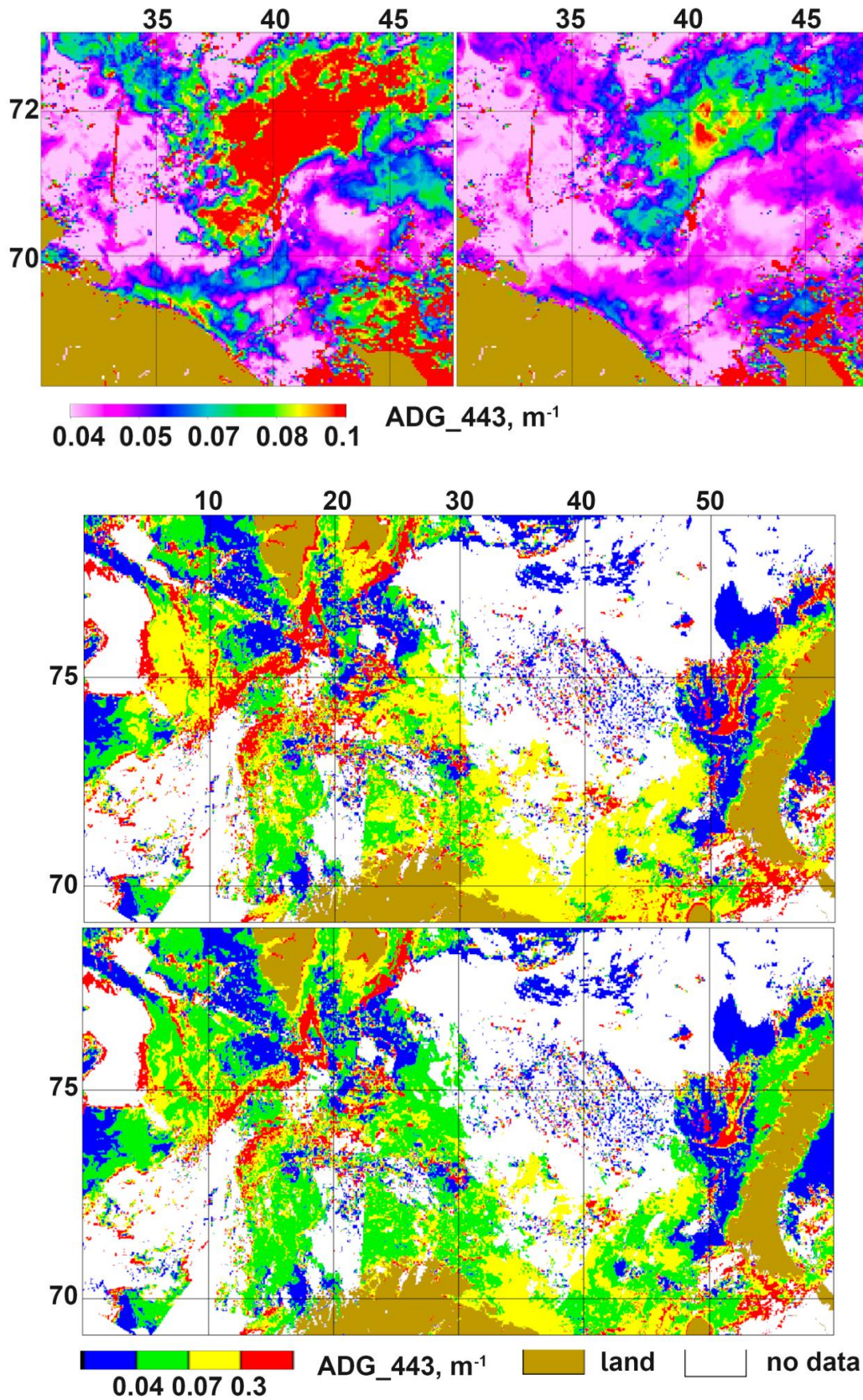


Figure 6.A The ADG₄₄₃ distributions based on standard OLCI data ag_OLCI_standard (left) and corrected ag_corr data (right) for the AMK-65 cruise. B. The same for the AMK-68 cruise.

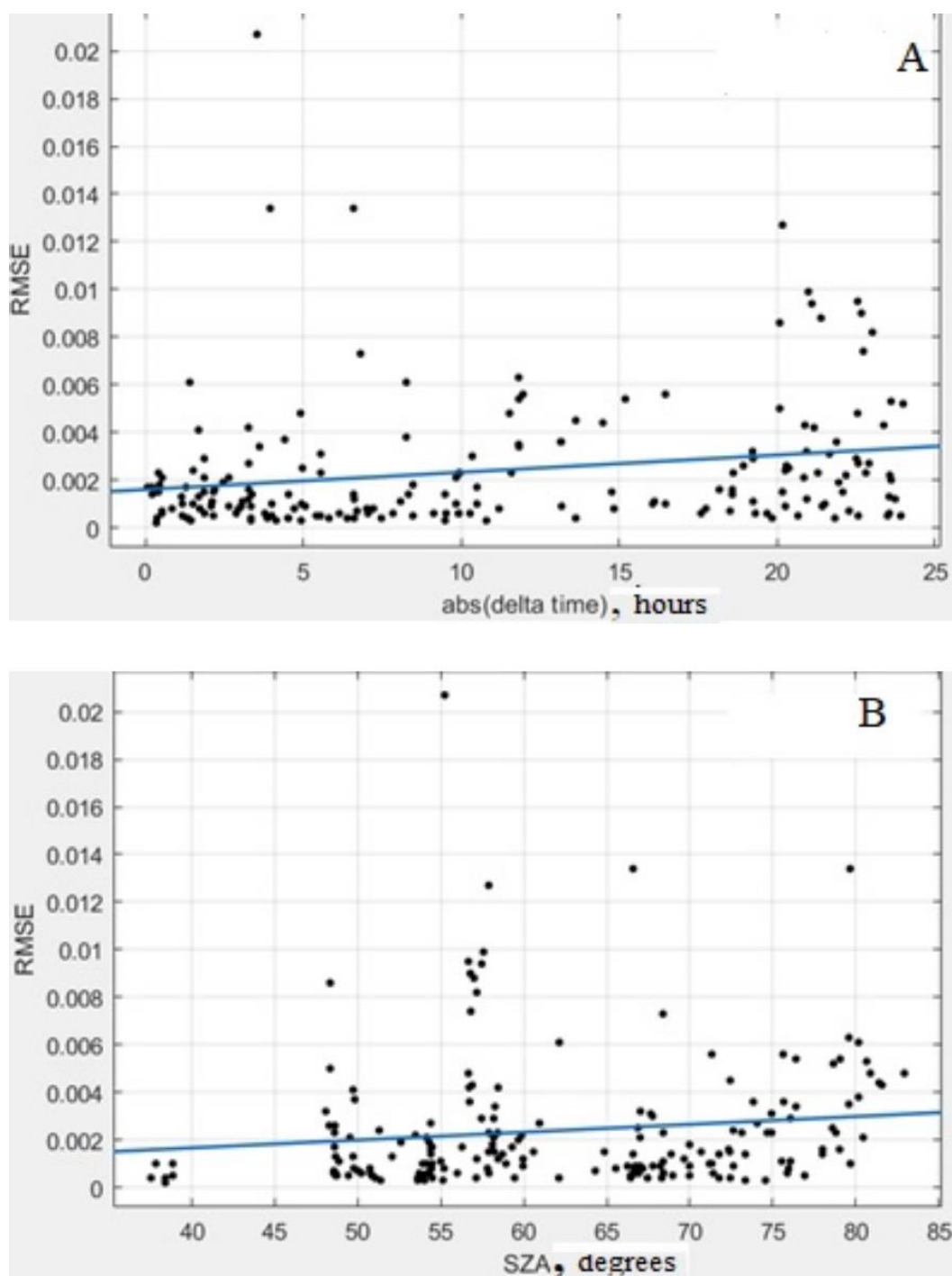


Figure 7. Dependences of the RMSE of the R_{rs} values on the difference between the time of the in situ and the satellite measurements (A) and on the zenith angle of the Sun (B). The blue lines show the trend assessment.

The errors increase at the angles $> 75^\circ$. For the entire dataset ($N = 189$), there are no significant dependencies: the coefficient of determination $R^2 = 0.043$ for the module of the time interval at a significance level of $p = 0.004$, and $R^2 = 0.016$, $p = 0.083$ for the solar zenith angle. The absence of a relationship between the error magnitude and the time interval between shipboard and satellite data indicates the stability of the measurement conditions due to the hydrometeorological factors and oceanological processes prevailing in the period under consideration. Nevertheless, at intervals exceeding 20 hours, the errors increase by a factor of 1.5 (RMSE for time difference > 20 hours equals 0.0036 while the mean RMSE = 0.0024, $N = 48$). This is related to the surface water dynamics [42].

For further analysis, we chose only satellite spectra with the $RMSE \leq 0.001$.

It is worth noting that in the Kara and Laptev Seas, the strong influence of river runoff leads to a decrease in the water-leaving radiation values in the short-wavelength part of the spectrum due to absorption by dissolved organic matter, which increases the errors in the determination of the absorption coefficient ADG_{443} . As an example, Figure 8 shows all the R_{rs} spectra for station 6240, performed in the Kara Sea on July 14, 2019. For this station, we collected the most significant amount of satellite data - 23 files. The colors show the data of the various sensors; black line – the result of direct determinations; gray lines – the spectra with the $RMSE > 0.001$.

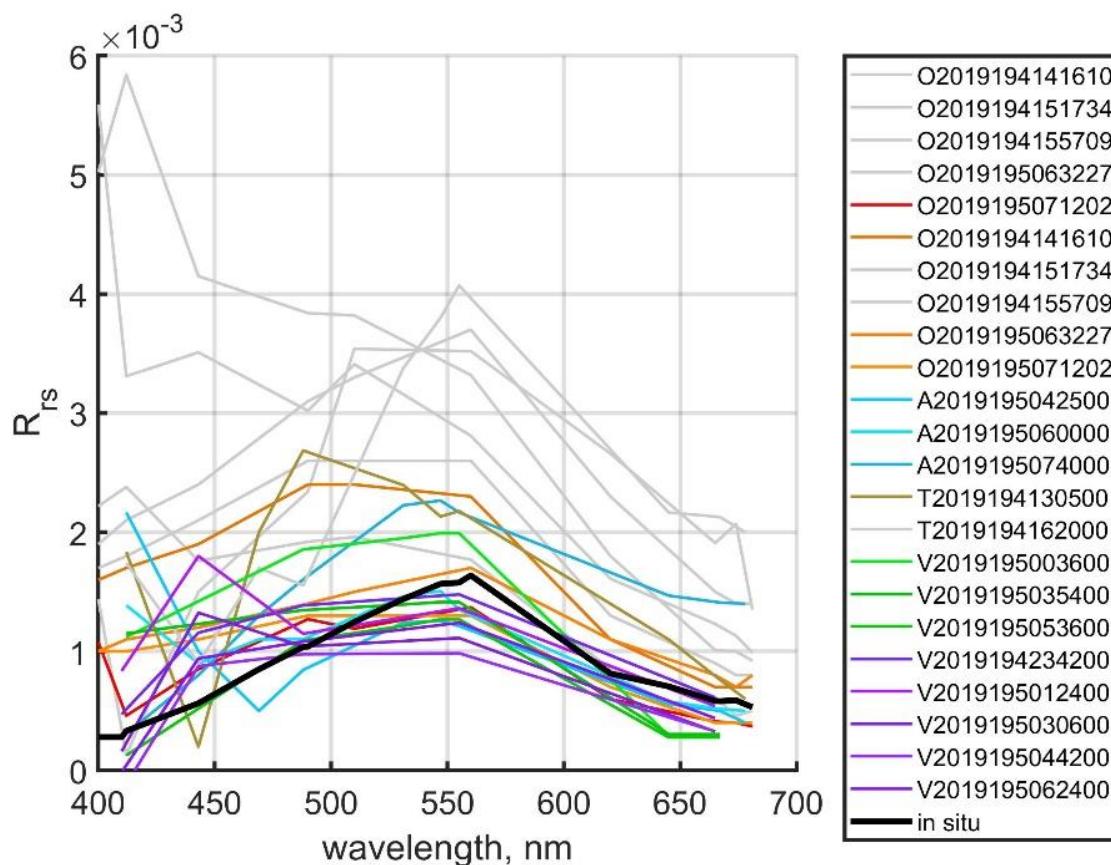


Figure 8. $R_{rs}(\lambda)$ values obtained from the results of shipboard (black line) and satellite measurements (colored lines: red – OLCI BAC, orange – OLCI AAC, blue – MODIS Aqua, brown – MODIS Terra, green – VIIRS SNPP, purple – VIIRS NOAA-20). Grey color shows data for which the RMSE values obtained by comparing shipboard and satellite data are greater than 0.001. Station 6240, Kara Sea, July 14, 2019

Figure 9 demonstrates the variability of errors depending on the solar zenith angle (SZA) and the time interval between field measurements and the satellite overpass time.

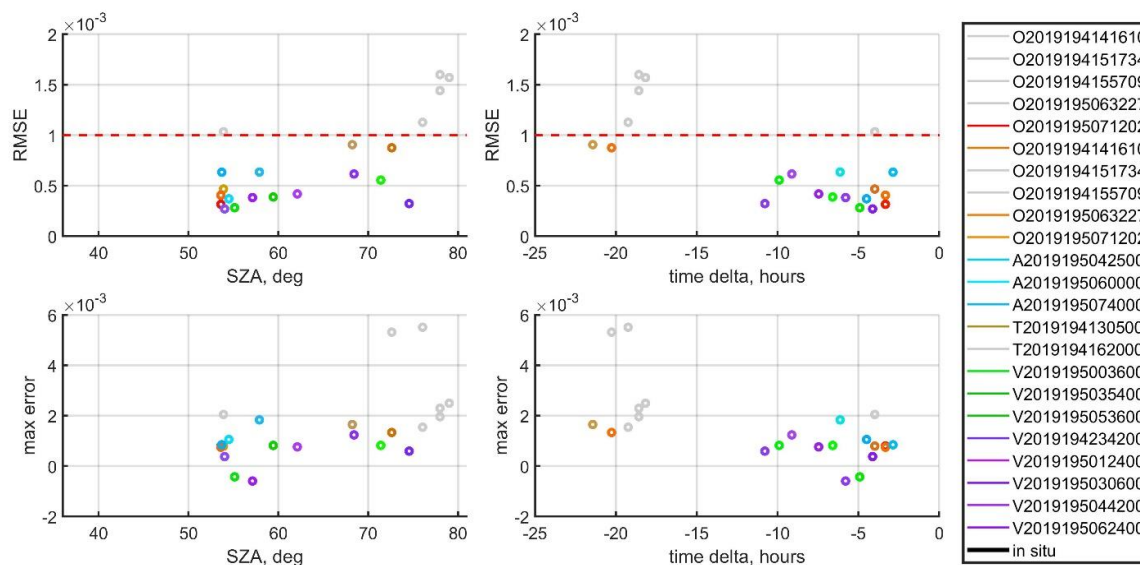


Figure 9. RMSE (top row) and maximum error (bottom row) values obtained when comparing shipboard and satellite data depending on the sun zenith angle (left column) and the time interval between data (right column). The colors of the circles correspond to the colors of the lines in Figure 1. The gray circles show the data for which the RMSE values exceed 0.001. The red dotted line on the right side of the figure corresponds to the RMSE = 0.001. Station 6240, Kara Sea, July 14, 2019

The spatial distribution of the beam attenuation coefficient c measured in the Kara Sea on the day of station 6240 (July 14, 2019) using the flow-through measuring complex is shown in Figure 10.

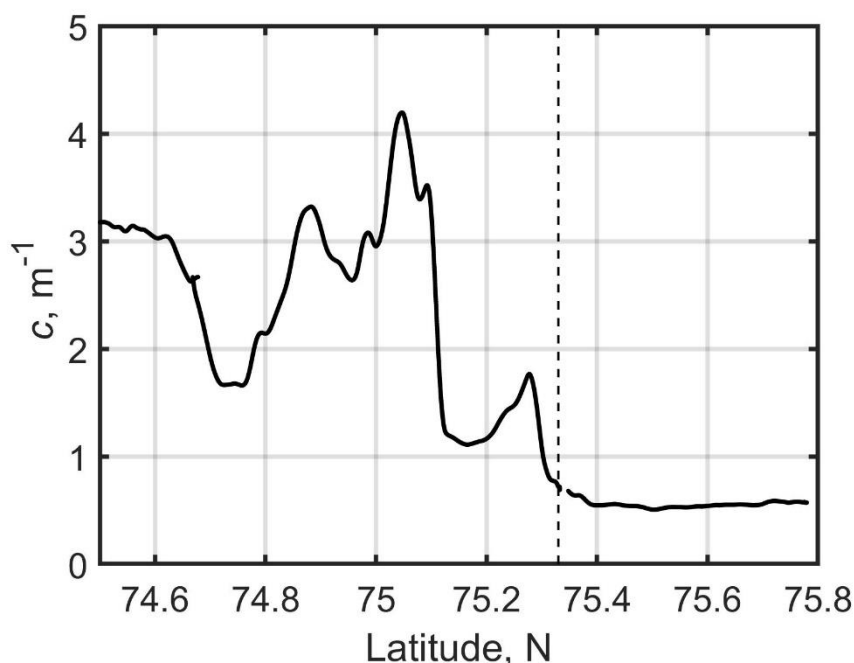


Figure 10. Spatial distribution of the beam attenuation coefficient c measured in the Kara Sea on July 14, 2019. The dotted line shows the position of station 6240.

The values of $c(532)$ exceeding 1 m^{-1} correspond to the waters of the surface desalinated layer formed in the summer season by the Ob and Yenisei river runoff [43]. These waters are characterized

by lower salinity values and a high content of colored dissolved organic matter (CDOM) compared to waters outside the influence of river runoff [42]. Station 6240 is located in the area where waters with different optical characteristics come into contact, which causes the observed differences in the values of the absorption coefficient, calculated using different algorithms from different data.

Comparison of the total amount of satellite data for the stations, where the shipboard reflectance measurements were carried out, with the amount of data remaining after applying the criterion for standard error values $RMSE < 0.001$ for all used ocean color scanners is presented in Table 5. It should be noted that the results of the OLCI AAC better match to shipboard data (13 spectra out of 27 remained) than the results of BAC correction (3 spectra out of 27 remained).

Table 5. Amount of satellite data for 15 stations, where shipboard reflectance measurements were carried out. AAC – Alternative Atmospheric Correction, BAC – Baseline Atmospheric Correction.

Sensor	All data	$RMSE \leq 0.001$
OLCI BAC	27	3
OLCI AAC	27	13
MODIS Aqua	36	16
MODIS Terra	40	13
VIIRS SNPP	37	14
VIIRS NOAA-20	22	18

Figure 11 shows the RMSE values for all 27 OLCI spectra obtained using the alternative atmospheric correction, depending on the solar and viewing zenith angles, as well as the difference in the azimuthal angles. Flags are marked with symbols. There is a little amount of data without flags – only six spectra. That indicates unfavorable conditions for satellite observations in the studied seas. The most frequent flag is the ‘cloud risk’ (12 points), the ‘sun glint risk’ flag is observed at four locations, all other flags at five. The errors increase at the solar azimuthal angles more 75° , and the viewing angles greater than 15° . It should be noted that the risk of cloudiness or glint does not always lead to errors.

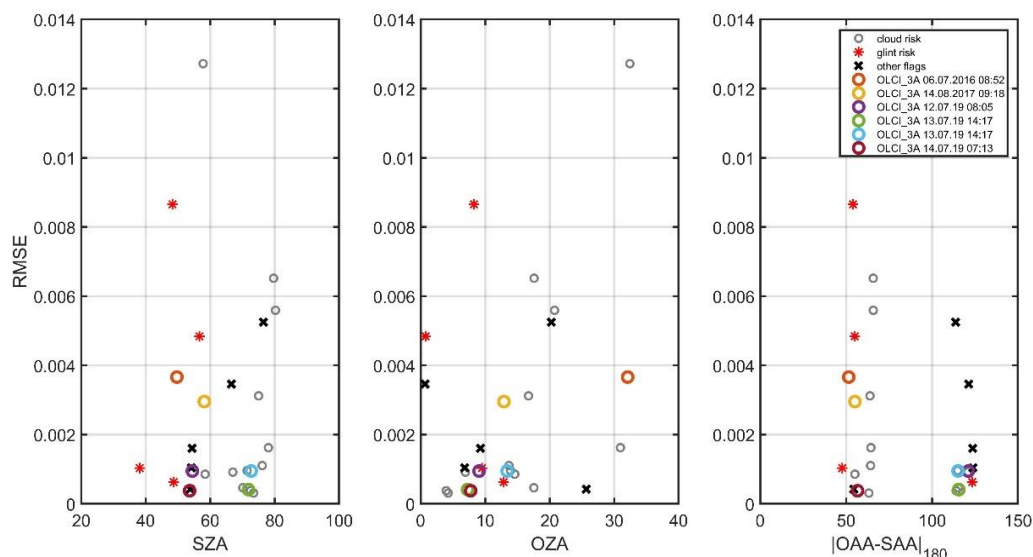


Figure 11. RMSE values obtained by comparing shipboard and satellite data for 15 ship stations and 27 OLCI spectra calculated using C2RCC processor, depending on the solar zenith angle (left), observation zenith angle (center) and azimuth angles difference (right). Gray circles indicates the cloud risk flag, red asterisks – glint risk, black crosses – any other flag, colored circles – data without flags.

3.3 OLCI estimates of the particle backscattering coefficient

3.3.1 In situ measurements in the Barents Sea

In this section, we consider the measured data from the AMK-65 and AMK-68 cruises. The particle backscattering coefficient b_{bp} values were not directly measured in our field studies. The b_{bp} values were calculated using the R_{rs} values, measured by a floating (AMK-65) and a deck (AMK-68) spectroradiometers; the calculations were made for a wavelength of 555 nm using the different algorithms described in 2.2.2: the simplified regression algorithm (RSA) [23]; a quasi-analytical algorithm QAA [22], and the model of the optical properties of seawater - GIOP (Generalized Inherent Optical Property) [33, 34].

The b_{bp} (555) data for the selected stations were compared with the attenuation coefficient c , m^{-1} data for the subsurface layer (5 m). Direct determinations obtain the c (m^{-1}) data with the PUM-A device (Section 2). Figure 12 shows the results of the comparison of the $b_{bp}(555)$ values using different algorithms and c (m^{-1}) measured in situ.

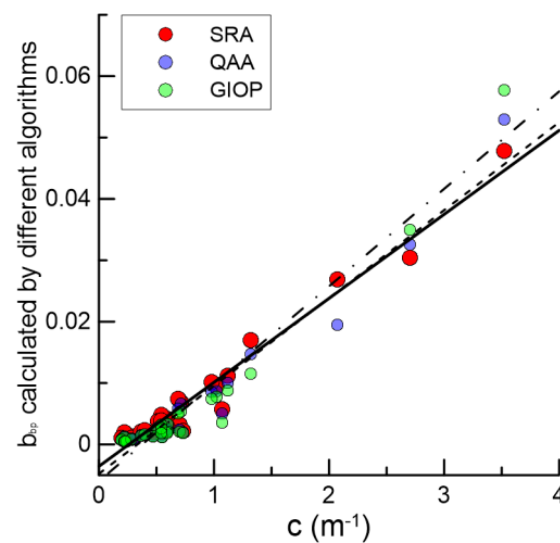


Figure 12 Comparison of the backscattering coefficient of particles b_{bp} (555) with attenuation coefficient c (m^{-1}) data for the Barents Sea. Red circles – SRS algorithm, blue - QAA algorithm, green - GIOP algorithm. Black line is a correlation based on SRA, black dotted line - correlation based on QAA data, dash-dotted line - based on GIOP data.

Table 6 presents the statistical parameters of the regression of the backscattering coefficient of particles b_{bp} (555) through the values of the attenuation coefficient c (m^{-1}) for different algorithms.

Table 6. The parameters of the regression of the particle backscattering coefficient $b_{bp}(555)$ (Y) through the values of the attenuation coefficient c (m^{-1}) (X) using different algorithms.

Algorithm	n	Regression	$\langle X \rangle$	$\langle Y \rangle$	R^2	RMSE, m^{-1}	RE, %
RSA	31	$Y = 0.01 X - 0.004$	0.78	0.01	0.96	0.0020	29
QAA	31	$Y = 0.014 X - 0.005$	0.78	0.01	0.95	0.0026	40
GIOP	29	$Y = 0.02 X - 0.006$	0.75	0.005	0.94	0.0031	51

N – number pairs to calculate regression, R^2 – determination coefficient, RMSE – Root Mean Square Error, RE – average relative error

Figure 12 and Table 6 show a good agreement between the b_{bp} (555) and the c (m^{-1}) values: the coefficient of determination $R^2 = 0.95$, $R^2 = 0.94$ for the QAA and GIOP algorithms respectively, and $R^2 = 0.96$ for RSA.

3.3.2. Comparison of the particle backscattering coefficient values derived from field and OLCI satellite data

Stations were selected in the Barents and the Kara Seas at the AMK-65, 68, 72, and 76 cruises for comparing the b_{bp} data derived from field and OLCI satellite data. The stations included the data from a floating or a deck spectroradiometer, satellite data from OLCI, MODIS and VIIRS, and absorption data measured by ICAM. Stations 6240 and 6229_2 of the AMK-76 cruise were removed from the consideration (see 3.1, 3.2). For OLCI data, the calculation was performed using the R_{rs} values available as the results of the BAS (standard) and AAS (NN) atmospheric correction. In the last case, the R_{rs} data of the 2nd level were derived from the TOA Level 1 radiance data, using the C2RCC processor of the SNAP program [32]. For the calculations in the Kara Sea, the regional semi-analytical RSA was also used. Figure 13 shows the regression lines for the Barents (a), the Kara and Laptev seas (b). Table 7 presents the parameters for different regions, algorithms, and satellites.

In the Kara Sea, a correlation with $R^2 > 0.3$ is observed only in the case of the C2RSS processor, the QAA algorithm. That may be due to the strong influence of river flow in this region. A better correlation is observed for stations in the Barents Sea. For example, for standard OLCI level 2 data using the GIOP algorithm, $R^2 = 0.92$.

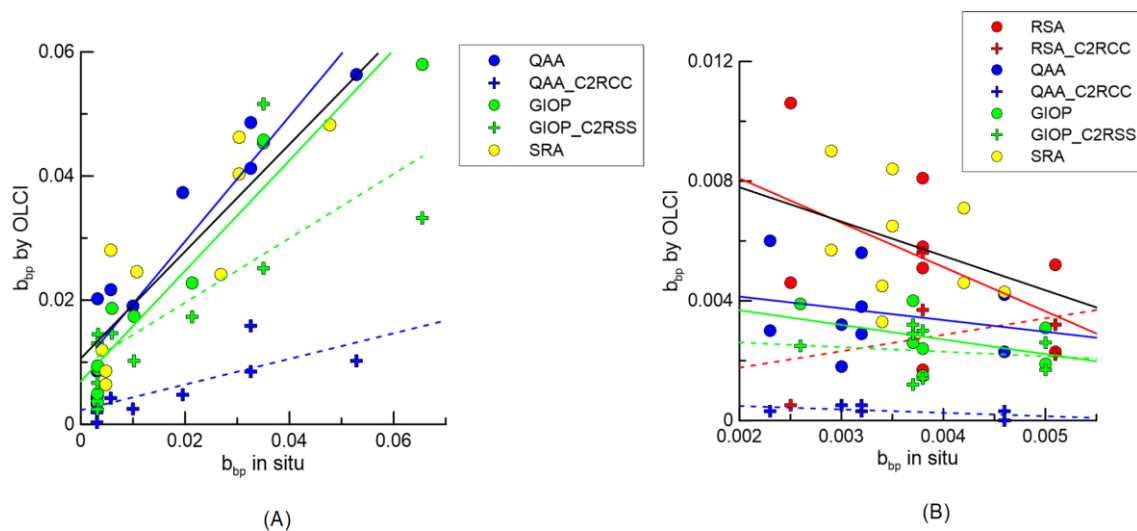


Figure 13. Comparison of b_{bp} (555) in situ and satellite calculations for the Barents Sea (a), the Kara Sea and the Laptev Sea (b). Red circles - RSA algorithm of the 2nd level data, red crosses - RSA_C2RCC algorithm; blue circles - QAA algorithm for data of the 2nd level, blue crosses - QAA_C2RCC algorithm; green circles - GIOP algorithm for data of the 2nd level, green crosses - GIOP_C2RCC algorithm; yellow circles - SRA. Straight lines - direct correlation - match the colors of the second-level algorithms, dashed lines - for C2RSS algorithms, black straight - for RSA

Table 7. Regression parameters between $b_{bp}(555)$ from satellite (Y) and ship (X) data for different algorithms (only cases are presented where the values of the determination coefficient exceed 0.3; in other cases shown in Figure 3.3.2 there is no significant correlation).

Algorithm X	Algorithm m Y	Seas	n	Regression	$\langle X \rangle$	$\langle Y \rangle$	R^2	RMSE, m^{-1}	RE, %
QAA	Standard	Barents	11	$Y = 1.01 X + 0.01$	0.02	0.03	0.87	0.0072	28
QAA	C2RCC	Barents	11	$Y = 0.21 X + 0.002$	0.02	0.005	0.61	0.0031	54
QAA	C2RCC	Kara and Laptev	9	$Y = -0.11 X + 0.001$	0.003	0.0003	0.33	0.0002	56
GIOP	Standard	Barents	11	$Y = 0.89 X + 0.01$	0.02	0.02	0.92	0.0059	26
GIOP	C2RCC	Barents	11	$Y = 0.52 X + 0.01$	0.02	0.02	0.56	0.0102	54
RSA	RSA	Barents	11	$Y = 0.86 X + 0.01$	0.02	0.03	0.75	0.0084	32

3.4. Diffuse attenuation coefficient

3.4.1. Comparison of a_g and K_d measured in situ

Figure 14 shows the results of comparison between the values of $a_g(443)$ and $K_d(443)$ measured in situ, separately for the Barents and Norwegian Seas (AMK 68 – Figure 14A) and the Kara Sea (AMK 72 and 76 - Figure 14.B) The a_g coefficient was measured using ICAM, K_d was calculated from the data of the underwater irradiance measured by two instruments (BIC and Ramses) in the upper homogeneous layer. If measurements for the station were made with both instruments, then the K_d coefficient was determined as the average between these measurements.

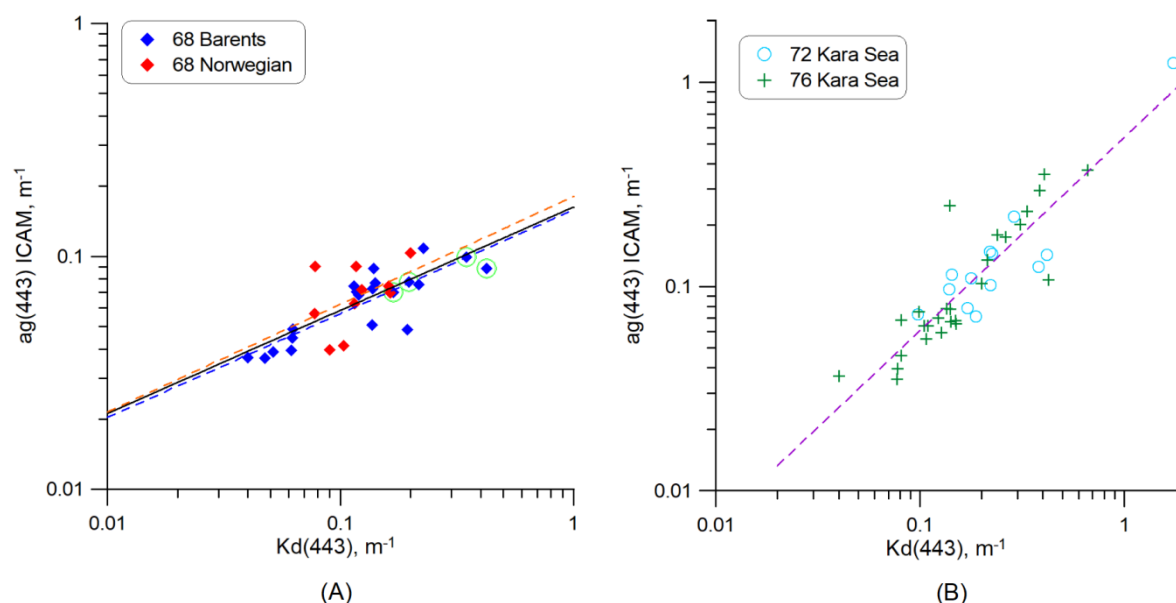


Figure 14. Comparison of the yellow substance absorption coefficient $a_g(443)$ and diffuse attenuation coefficient $K_d(443)$ measured in situ: (A) for the Barents and Norwegian Seas (AMK 68); (B) the Kara Sea (AMK 72 and 76). Black solid line is regression line for all AMK 68 data; blue dotted line - the Barents Sea, AMK 68; red dotted line - the Norwegian Sea, AMK 68; purple dotted line – the Kara Sea, AMK 72 and 76. Green circles show the stations with coccolithophore blooms.

Table 8 presents the parameters of the regression between the values $a_g(443)$ and $K_d(443)$. It can be seen that a reasonably good correlation is seen for the Kara Sea, with data from the cruises AMK 72 and 76: the coefficient of determination $R^2 = 0.73$. For the Barents Sea, we also get a high correlation ($R^2 = 0.72$), but the regression equations in these two seas differ significantly. At the same time, the stations with coccolithophore blooms (see Figure 14A) fit well into the obtained regression. For the waters of the Norwegian Sea, there is no stable relationship between $a_g(443)$ and $K_d(443)$: $R^2 = 0.21$, but the resulting regression equation does not differ much from that obtained for the Barents Sea. The results obtained indicate the consistency of measurements of a_g and K_d .

Table 8. Regression parameters between values of a_g and K_d measures in situ for wavelengths 443 nm.

Data set	N*	Regression equation	R^2
Barents Sea, AMK 68	20	$a_g = 0.16 K_d^{0.44}$	0.72
Norwegian Sea, AMK 68	10	$a_g = 0.18 K_d^{0.46}$	0.21
all AMK 68 data	30	$a_g = 0.16 K_d^{0.44}$	0.56
Kara Sea, AMK 72 and 76	31	$a_g = 0.55 K_d^{0.94}$	0.73

*N, the number of pairs to calculate regression; R^2 , the coefficient of determination

3.4.2. Consistency between the data derived from field measurements

For checking the consistency of the field measurements, we calculated K_d using a simple formula: $K_d = (1+0.005 \theta_0) a + 3.47 b_b$, where a and b_b - the seawater absorption and backscattering coefficients, θ_0 - the solar zenith angle [44]. This formula provides reasonable accuracy for waters with coccolithophore bloom and no bloom [45].

We use the spectral values of the absorption coefficient $a(\lambda)$, measured by ICAM, and the backscattering coefficient determined as the sum of the scattering by the particles and pure water, the particles backscattering b_{bp} was calculated from the in situ measured spectra $R_{rs}(\lambda)$ using the algorithm [41].

The correspondence of the K_d values calculated by formula [44] and based on in situ measurements of underwater irradiance for 18 stations in the Barents Sea (AMK 68) is shown for two wavelengths 443 and 490 nm in Figure 15. It is seen an excellent agreement of the K_d estimates obtained for both spectral channels: in both cases, the coefficient of determination is $R^2 = 0.98$; The RMSE equal to 0.028 and 0.035 m^{-1} for 443 and 490 nm, respectively. The stations with coccolithophore blooms do not worsen the obtained correspondence. That proves a good agreement between the data of our field measurements of the absorption coefficient $a(\lambda)$, remote sensing reflectance spectra $R_{rs}(\lambda)$, and the diffuse attenuation coefficient $K_d(\lambda)$.

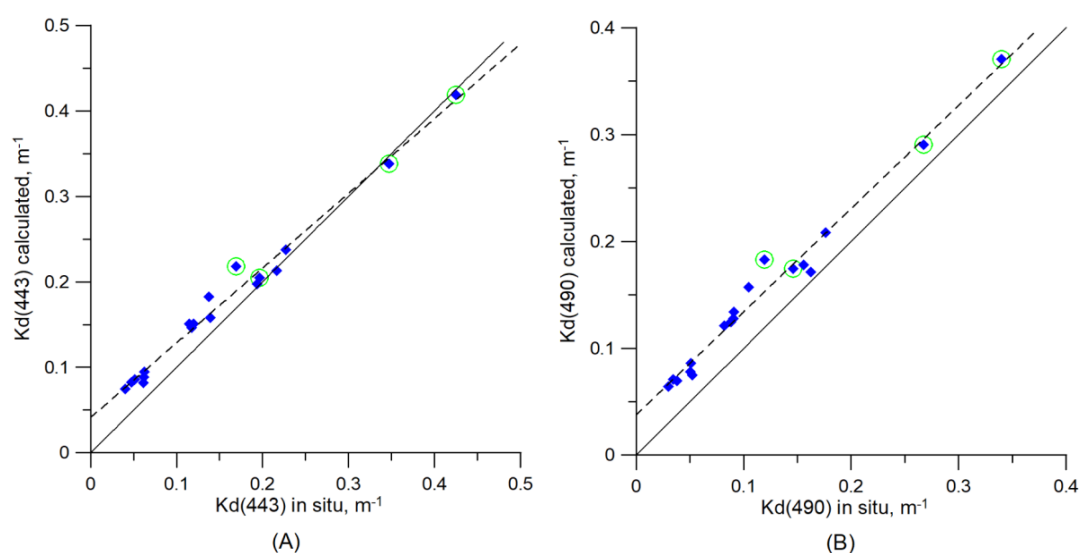


Figure 15. Scatterplot of diffuse attenuation coefficient K_d calculated by formula [44] and on the basis of in situ measurements of underwater irradiance for stations in the Barents Sea (AMK 68) and two wavelengths 443 (A) and 490 (B) nm. Black solid line - perfect correspondence 1:1; black dotted line - linear regression. Green circles show the stations with coccolithophore blooms.

3.4.3. Comparison of $K_d(490)$ values from satellite and field data (standard algorithms)

Figure 16 presents the results of the comparison between the values of diffuse attenuation coefficient $K_d(490)$ calculated from the data of field measurements and the OLCI data obtained as a level 2 standard product. The $K_d(490)$ value in the nearest pixel is used, but only for those satellite overpasses with the number of valid pixels at least 17 out of 25 closest. Some stations have more the overpasses than others; the maximum number (9) was received for station 6239 in the Kara Sea (AMK 76, $K_d(490) = 0.32 m^{-1}$ according to in situ data). As seen, almost all OLCI flights gave the underestimated $K_d(490)$ values (0.10-0.15 m^{-1}); only the OLCI flight, closest by the time of the field measurements (less than 4 hours), gave $K_d(490) = 0.39 m^{-1}$.

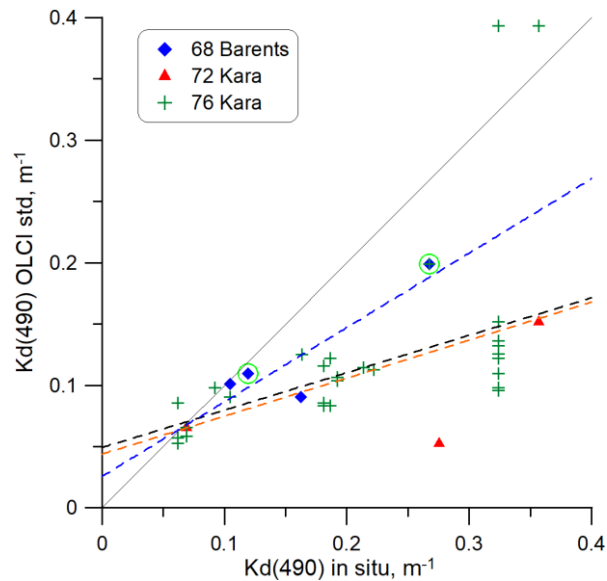


Figure 16. Scatterplot of diffuse attenuation coefficient $K_d(490)$ calculated from field measurements and OLCI data (standard algorithm, nearest pixel). Black solid line - perfect correspondence 1:1; black dotted line - regression line for all data; blue dotted line - the Barents Sea, AMK 68; red dotted line - the Kara Sea, AMK 72 and 76. Green circles show the stations with coccolithophore blooms.

Table 9 shows the parameters of the correspondence between the $K_d(490)$ values calculated from OLCI and field data if we use satellite data for the nearest pixel. As seen, from Figure 16 and Table 9, a good agreement between satellite and field data is observed for the Barents Sea (AMK 68): coefficient of determination $R^2 = 0.76$, a standard error $RMSE = 0.05 \text{ m}^{-1}$, the relative error $RE = 20\%$. But these calculations were carried out only for 4 stations. The stations with coccolithophore bloom did not show much difference from other stations in this region.

In the Kara Sea (AMK 72 and 76), in general, the satellite values of $K_d(490)$ are approximately two times lower than $K_d(490)$ obtained from in situ measurements: the ratio of the mean values is 0.54, $RE = 45\%$, but for stations in clear waters with $K_d(490) < 0.1 \text{ m}^{-1}$ satellite data errors do not exceed 15%.

Table 9. Correspondence parameters between the $K_d(490)$ values obtained from field measurements (X) and from OLCI data (Y). Satellite data are taken for the nearest pixel.

Data set	Regression equation	N*	R^2	$\langle Y \rangle / \langle X \rangle$	RMSE	RE
AMK 68	$Y = 0.61 X + 0.03$	4	0.80	0.76	0.05	20%
AMK 72 и 76	$Y = 0.31 X + 0.04$	24	0.24	0.51	0.14	45%
All data	$Y = 0.31 X + 0.05$	28	0.24	0.54	0.13	42%

N, the number of pairs; R^2 , the coefficient of determination; $\langle Y \rangle / \langle X \rangle$, the ratio of mean $K_d(490)$ values; RMSE, the root mean squared error, m^{-1} ; RE, the relative error

Figure 17 shows the correspondence between the values of diffuse attenuation coefficient $K_d(490)$ calculated from field measurements and satellite data (MODIS and VIIRS). As in the case of OLCI, the $K_d(490)$ values are obtained from level 2 files, so they are the standard product of these scanners. The $K_d(490)$ values in the nearest pixel are used. Since the time of overpass of the considered satellites differs from each other, the set of presented data for each scanner is different. Unlike OLCI, for MODIS and VIIRS scanners, we managed to obtain data for station 5580 in the Barents Sea with an intense coccolithophore bloom observed (directly measured concentration of the coccolithophore plated cells was approximately $5 \times 10^6 \text{ cell/L}$, the detached coccoliths $1.5 \cdot 10^8 \text{ cell/L}$), and $K_d(490) = 0.34 \text{ m}^{-1}$.

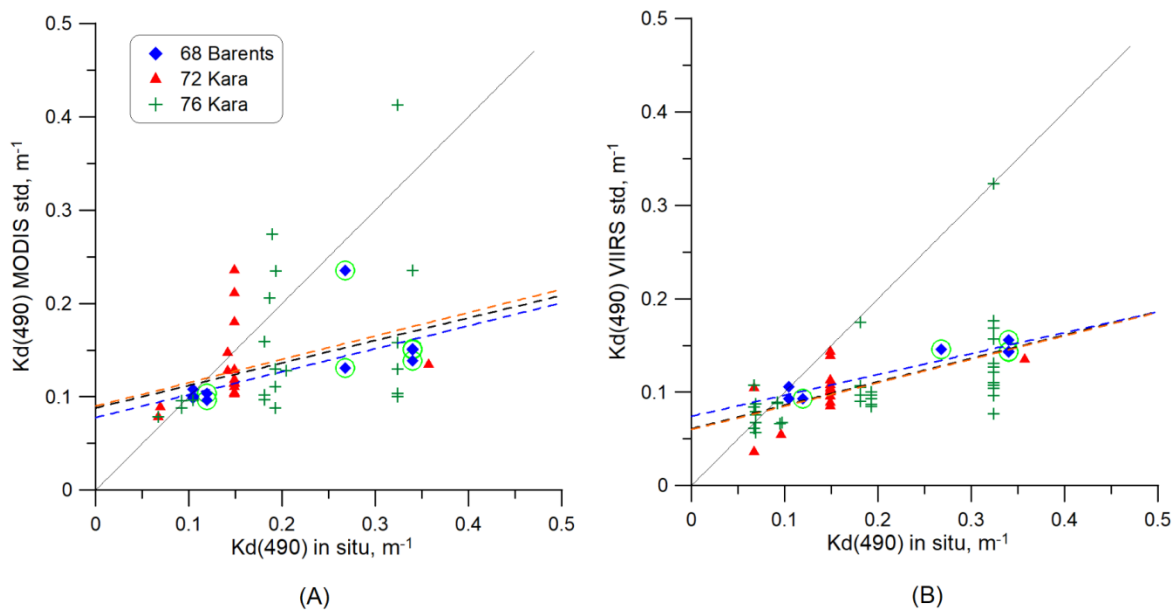


Figure 17. Scatterplot of diffuse attenuation coefficient $K_d(490)$ calculated from field measurements and satellite data (standard algorithm, nearest pixel): (A) MODIS; (B) VIIRS. Black solid line - perfect correspondence 1:1; black dotted line - regression line for all data; blue dotted line - the Barents Sea, AMK 68; red dotted line - the Kara Sea, AMK 72 and 76. Green circles show the stations with coccolithophore blooms.

Table 10 shows the parameters of the correspondence between the $K_d(490)$ values from satellite (MODIS and VIIRS) and field data if satellite data are used for the nearest pixel. The calculated parameters are almost the same for both scanners and depend little on the region: the regression equations are practically the same, and the errors also. The satellite estimates of $K_d(490)$ reasonably coincide with field data in clear waters, where $K_d(490) < 0.2 \text{ m}^{-1}$, and give underestimates in more turbid waters, which are the result of the influence of intense coccolithophore bloom in the Barents Sea, and the river runoff in the Kara Sea.

Table 10. Correspondence parameters between the $K_d(490)$ values obtained from field measurements (X) and from satellite data (Y). Satellite data are taken for the nearest pixel. All parameters are the same as in Table 9.

Data set	Regression equation	N	R ²	$\langle Y \rangle / \langle X \rangle$	RMSE	RE
MODIS						
AMK 68	$Y = 0.25 X + 0.08$	13	0.48	0.63	0.11	26%
AMK 72 и 76	$Y = 0.25 X + 0.09$	32	0.09	0.74	0.09	33%
All data	$Y = 0.24 X + 0.09$	45	0.14	0.70	0.10	31%
VIIRS						
AMK 68	$Y = 0.22 X + 0.07$	7	0.91	0.55	0.13	36%
AMK 72 и 76	$Y = 0.25 X + 0.06$	49	0.31	0.58	0.14	47%
All data	$Y = 0.25 X + 0.06$	56	0.35	0.57	0.14	45%

If we compare the $K_d(490)$ estimates from the OLCI data with the MODIS and VIIRS estimates, then for all three scanners a good agreement with the field data is obtained in clear waters ($K_d(490) < 0.2 \text{ m}^{-1}$), and in more turbid waters they underestimate the $K_d(490)$ value by about a factor of 2.

4. Discussion

Specialists in the various scientific and engineering directions, using satellite data, need to know the uncertainties in the end product, not only the errors in measurement and retrieval of the geophysical parameter used. The goal of our study is to assess the real possibilities of evaluating the absorption of seawater and colored organic matter using OLCI satellite scanner data in the northern waters - the Barents Sea (partly, the Norwegian Sea) and the Kara sea (partly, the Laptev Sea). Our possibility to reach the above goal is based on the availability of the appropriate data from field measurements in five expedition voyages of the R/V *Akademik Mstislav Keldysh* (SIO RAS) in the period 2016 -2019.

As we mentioned in the Introduction, the conditions for obtaining satellite data in the Arctic Basin are extremely unfavorable, and in such situations, the real uncertainties may differ significantly from the errors of the instrumental measurements and the parameter retrieval by the developed algorithms. An essential advantage of the OLCI data products is that it provides the user not only the data files with the error estimates but the annotations data files comprising the classification, Water Quality, and Science Flags (WQSF). The WQSF file provides information about the validity and suspicious quality; Level-1B products contain atmospheric and meteorological data, solar and satellite angles.

We executed our study by applying the comprehensive approach based on the analysis of multi-sensor and multi-variable data from satellite and in situ measurements. Our analysis included satellite data from OLCI Sentinel-3A and 3B, MODIS Aqua and MODIS-Terra, VIIRS SNPP, and VIIRS NOAA-20 from 2016 to 2019, and the field data on the spectral absorption coefficients of seawater and the colored organic matter, the spectral remote sensing reflectance above and beneath sea surface, the spectral diffused attenuation coefficient, the beam attenuation coefficient. For calculating the inherent optical properties (IOP) from remote sensing data, primarily for calculating the absorption coefficients, the backscattering coefficient, and TSM concentration, we used the different algorithms.

In particular, we compared the OLCI ADG443_NN values obtained as a standard Level 2 product and derived by the C2RCC neural network processor of the SNAP program, developed by the European Space Agency (ESA) [[31,32]. We also performed such a comparison for the spectral remote sensing reflectance values R_{rs} values derived by the Baseline Atmospheric Correction algorithm (BAC reflectance) and by Alternative Atmospheric Correction algorithm based on a neural network procedure (AAC reflectance). To estimate the uncertainties and assess the real possibilities of evaluating the absorption of colored organic matter from OLCI data, we directly compared the OLCI ADG443_NN values with the directly measured values of the yellow substance absorption coefficient a_g .

Figures 18 demonstrate the results of such comparison, as compared with the standard product ADG_443_NN (OLCH file S3A_OL_2_WFR_20170814T091713), the Barents Sea, 14 August 2017. Figures 18 A, B shows the scatterplots of the calculated errors the ADG443_NN_err in depending on the absolute values ADG443_NN for a single OLCI file of 14 August 2017 (on different scales). As seen, the average relative error equal to ~10 %, the maximum values d not exceed 30 %.

Figures 18 C, D show the results of the comparison between the values of ADG_443_NN (a_{olci_std}) and the in situ measured by the ICAM spectrophotometer. Fig. 18 C presents data for the complete dataset (151 pairs), including the estuaries of the Ob and Yenisei rivers, Fig. 18 D – for 89 pairs after the rejection of the river mouths, as well as stations with large zenith angles of the sun (more than

750) and other factors that impede obtaining quality data. As seen, the errors in the last case can reach 100% and even more.

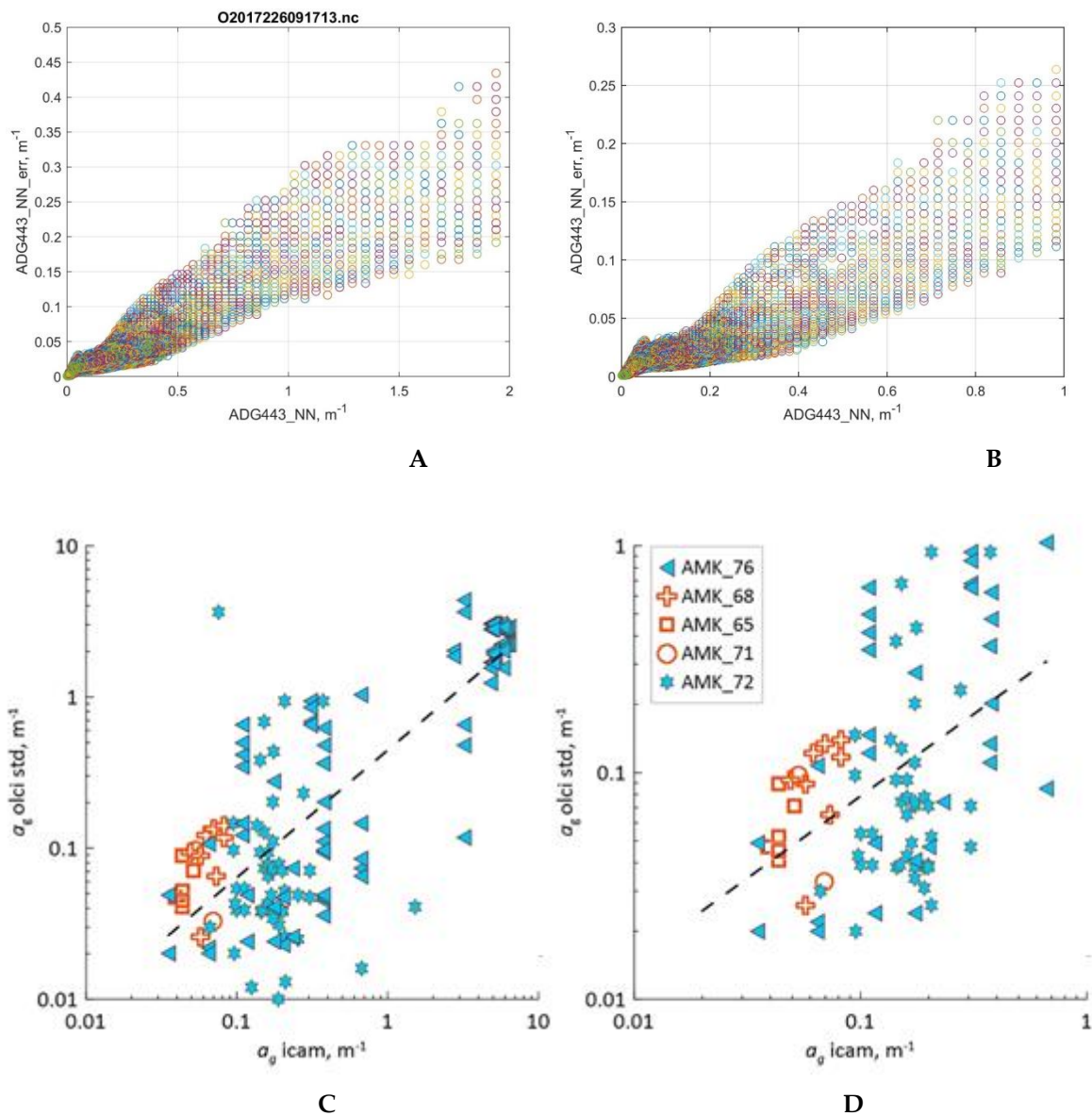


Figure 18 The errors in the ADG_443_NN values, the Barents Sea:

A, B – standard product for OLCI file S3A_OL_2_WFR_20170814T091713, the Barents Sea, 14 August 2017;

C, D – comparison between the ADG_443_NN (a_{olci_std}) and the ICAM measured values. **C** - complete dataset, **D** - river estuaries excluded (see pp.10-11).

The bad observation conditions are the main factor determining a significant loss of data entirely or in their quality. In section 2.1, Figure 2 shows the distributions of the number of days with data for each bin and cloud coverage following the OLCI_CLOUD flags for AMK-65, 68, and 76 expeditions, averaged over the periods of study. There are the bins with no pixel with data over the whole expedition period; the numbers of the day with at least one pixel per bin in the most of the Barents Sea did not exceed 6. The cloud coverage maps, according to the OLCI_CLOUD flag, characterize the cloud coverage distributions over the study period.

Figure 18C shows, if we take the value of $0,02 \text{ m}^{-1}$ as an absolute error for the values $a_{\text{olci_std}}$ less than 0.1 m^{-1} , and 20% as a relative error for the values more than 0.1 m^{-1} , we must reject more than a half the total number pairs. The main reason for the appearance of bad points is unsatisfactory atmospheric correction. In section 3.2, we consider this problem in detail. As a parameter for analysis of the atmospheric correction errors, we used the values of the remote sensing reflectance R_{rs} . We selected 189 pairs of the $R_{rs}(\lambda)$ spectra for which a time difference between the in situ measurement and the satellite overpass did not exceed 24 hours. For each of the selected pairs, we calculated the standard deviation for the spectral difference between the spectra. We built the dependences of the RMSE values on the time difference and from the solar zenith angle. Analysis of these dependencies allows us to present the reasonable limitations relating to the further use of the satellite R_{rs} spectra: the $\text{RMSE} \leq 0.001$. This value is not a strict requirement; at present, we consider it as a reference point.

For analysis of the effectiveness of the retrieval OLCI ADG_NN, we selected 15 stations with acceptable atmospheric correction. Two of them were rejected due to other reasons, and we got 13 selected stations. For some of them, several Sentinel 3A, B passes were acceptable, and the total number of OLCI data used was 19 (10 for the Barents Sea, 9 for the Kara Sea). The main results of our work are formulated in Conclusions.

5. Conclusions

We conducted a comprehensive multi-sensor study of the uncertainties in satellite OLCI data on the color dissolved organic matter absorption under specific conditions of the Arctic Seas. For that, we used various approaches, comparing data from satellite (Sentinel-3 and four others) and field measurements in five sea expeditions 2016-2019, as well as different the data processing algorithms. The most significant, in our opinion, the results of the performed work, are presented below.

- First of all, we should note the significant losses in satellite data occur due to cloudiness, a frequent phenomenon in the Arctic region. That did not allow obtaining a full amount of data for our analysis, using a large number of in situ data measured in five sea expeditions. We managed to select, from the satellite ADG_443 spatial distributions for our cruises, only 151 pairs for the comparison. We shortened this set to 89 pairs after rejecting the Ob and Yenisei estuaries in the Kara Sea as well as stations with large zenith angles of the sun and other factors that impede obtaining quality data.
- The comparison of the OLCI ADG443_NN standard products with the directly measured by the ICAM spectrophotometer values of the yellow substance absorption coefficient a_g has shown that the real uncertainties of the final product quite different from the calculated errors the ADG443_NN_err. The former can exceed 100%, while the latter even for a single OLCI file, $\sim 10\%$. The main reason for that is the unsatisfactory atmospheric correction.
- An analysis of the atmospheric correction errors allowed us to select 19 pairs for further analysis (10 for the Barents Sea, 9 for the Kara Sea). For control, we also calculated the ADG_443 values using the L1 level OLCI data by the C2RCC processor of the SNAP program. We have derived the absorption coefficients, not only from OLCI data, but from other satellite sensors - MODIS-Aqua, MODIS-Terra; VIIRS SNPP, and VIIRS NOAA-20). We also used the different algorithms: QAA (Quasi-Analytical Algorithm) [22], SIORAS RSA (Regional Semi-analytical Algorithm) [23], GIOP (Generalized Inherent Optical Property) [33, 34].

For the OLCI standard product, a quite acceptable correlation was obtained only for the Barents Sea; for the Kara Sea it was insignificant. For the $a_g_{\text{OLCI_C2RCC}}$ values, a significant relationship was observed for both seas.

- We have derived the correcting equations a_g_{corr} vs. $a_g_{\text{olci_std}}$ and a_g_{corr} vs. a_g_{C2RCC} , allowing us to obtain the satellite absorption coefficient values closer corresponding to the measured ones. For the Barents Sea, we obtained reasonable results for the regression a_g_{corr} vs. $a_g_{\text{olci_std}}$: the coefficient of determination $R^2 = 0.670$, the regression error $s_{\text{regr}} = 0.030 \text{ m}^{-1}$, the

relative error (variation coefficient) RE = 55%. For the Kara Sea, there is not the acting equation for $ag_OLCI_standard$ due to the insignificance of the correlation. Still, it is possible for the absorption coefficient values calculated with the C2RCC processor: $R^2 = 0.624$, $s_{reg} = 0.045 \text{ m}^{-1}$, RE = 30%. Of course, the statistical support of the derived equations is insufficient, and we present them not for practical use.

- We have estimated the satellite atmospheric correction errors depending on the various factors, using the spectral radiance reflectance R_{rs} directly measured above the sea surface as a reference. The standard error RMSE increases weakly with increasing the time difference between the in situ measurement and the satellite overpass as well as on the solar zenith angle. Still, the RMSE values can be about 0.001 even though with a time difference of more than 20 hours and the solar zenith angles more 70° . Conversely, the errors exceeding 0.004 can be detected with a time difference of fewer than 5 hours and angles less than 50° . The other factors that affected RMSE are the azimuth angles difference and the situation in the surface water layer.

The number of the satellite spectra meeting the criterion $RMSE \leq 0.001$, is equal to 13 of 27 derived with the OLCI Alternative Atmospheric Correction (AAC_NN) and only 3 of 27 with the OLCI Baseline Atmospheric Correction (BAC). For comparison, the results for other satellite sensors are 13-18 from 36-40 for MODIS-Aqua, MODIS-Terra, and VIIRS SNPP, 18 of 22 for VIIRS NOAA-20.

- In our field studies, we did not directly measure the particle backscattering coefficient b_{bp} . We calculated the b_{bp} values using the R_{rs} values, measured by a floating (AMK-65) and a deck (AMK-68) spectroradiometers, and applied the different algorithms (the simplified regression algorithm (SRA) [41]), QAA [22], GIOP [33, 34]. For the Barents Sea, we checked the consistency of the $b_{bp}(555)$ data for the selected stations with values of the attenuation coefficient c , m^{-1} directly measured in the subsurface layer (5 m) by the PUM-device. For all algorithms, we found a good agreement between the $b_{bp}(555)$ and the $c(\text{m}^{-1})$ values: the coefficient of determination R^2 was equal to 0.95 (N=31) for the QAA, 0.94 (N=29) for GIOP, and 0.96 (N=31) for SRA.

- We have also got the results of a comparison between the b_{bp} values derived from field $R_{rs}(\lambda)$ data measured by a floating or a deck spectroradiometer and from OLCI satellite data. In the last case, the $R_{rs}(\lambda)$ data were obtained both as the results of the BAS (standard) and AAS (NN) atmospheric correction. The best results we obtained for the Barents Sea using the OLCI $R_{rs_standard}$ values and the QAA and GIOP algorithms: N=11, $R^2 = 0.87$ and 0.92 , $RMSE = 0.0072 \text{ m}^{-1}$ and 0.0059 m^{-1} , RE = 28 and 26%. For the Kara Sea, we have got the only result with the GIOP using the OLCI R_{rs_C2RCC} values: N=9, $R^2 = 0.33$, $RMSE = 0.0002 \text{ m}^{-1}$, RE = 56%.

- comparison of its values with the values of the diffuse attenuation coefficient $K_d(490)$ calculated from the data of field measurements. We found a good agreement between satellite and field data for the Barents Sea (AMK 68): coefficient of determination $R^2 = 0.76$, a standard error $RMSE = 0.05 \text{ m}^{-1}$, the relative error RE = 20% (but these calculations were carried out only for 4 stations). The stations with coccolithophore bloom did not show much difference from other stations in this region.

In the Kara Sea (AMK 72 and 76), in general, the satellite values of $K_d(490)$ were approximately two times lower than $K_d(490)$ obtained from in situ measurements: the ratio of the mean values was 0.54, RE = 45%, but for stations in clear waters with $K_d(490) \leq 0.1 \text{ m}^{-1}$ satellite data errors did not exceed 15%.

- For checking the consistency of the field measurements, we calculated K_d using a simple formula: $K_d = (1+0.005 \theta_0) a + 3.47 b_b$, where a and b_b - the seawater absorption and backscattering coefficients, θ_0 - the solar zenith angle [44]. This formula provides reasonable accuracy for waters with coccolithophore bloom and no bloom [45]. We used the spectral values of the absorption coefficient $a(\lambda)$, measured by ICAM, and the backscattering coefficient determined as the sum of the scattering by the particles and pure water, the particles backscattering b_{bp} was calculated from the in situ measured spectra $R_{rs}(\lambda)$ using the algorithm [41].

We have found an excellent agreement of the K_d estimates obtained for spectral channels of 443 and 490 nm for 18 stations in the Barents Sea (AMK 68): for both the wavelengths, $R^2 = 0.98$, the RMSE equals 0.028 and 0.035 m^{-1} for 443 and 490 nm, respectively. The stations with coccolithophore blooms do not worsen the obtained correspondence. This proves a good agreement between the data of our field measurements of the absorption coefficient $a(\lambda)$, remote sensing reflectance spectra $R_{rs}(\lambda)$, and the diffuse attenuation coefficient $K_d(\lambda)$.

- Because the absorption coefficient usually make a main contribution in the diffuse attenuation coefficient, it was interesting to check the correlation between these parameters. The a_g coefficient was measured using ICAM, K_d was calculated from the data of the underwater irradiance measured by the underwater spectroradiometers. For the Barents ($N=20$) and the Kara Sea, we have got the close values of R^2 equal to 0.72 and 0.73, but the regression equations in these two seas differ significantly. At the same time, the stations with coccolithophore blooms in the Barents Sea fit well into the obtained regression.

In our opinion, the most interesting and practically relevant results obtained in our work are related to the evaluation of the uncertainties in the retrieval of the absorption coefficient of the colored organic matter from satellite data in the real conditions of the Arctic seas. Some of the results should raise questions for specialists from the OLCI team. Why are the values of the absorption coefficient ADG_{443_NN} obtained as a standard product different from those calculated with the C2RCC processor, although, by the idea, both calculations should result in the same values? Our assessment showed that the apparent reason for such a difference is the unmatching results of atmospheric correction. Our data shows that the results from the C2RCC processor are better consistent with the data from field measurements. If this is the case, then perhaps it is possible to make appropriate changes in the calculation of the standard product?

A lack of appropriate satellite data for our validation studies was an unpleasant surprise for us. Having a large amount of field data, we have not expected that such a problem could arise. Now we see as the main task of our future work, the development of the statistically reliable method for assessment of the uncertainties in the retrieval of the bio-optical parameters from satellite data under the real conditions in the Arctic basin. We realize that such a problem requires the broader coverage of satellite data collecting combined with the field measurements, and it can be solved only by joint efforts of international cooperation.

Author Contributions: Conceptualization, O.Kopelevich; methodology, D.Glukhovets, O.Kopelevich; software, S. Sheberstov, D.Glukhovets; validation, D.Glukhovets, A.Yushmanova, S.Vasyulya, P.Karalli, I.Sahling; formal analysis, D.Glukhovets, A.Yushmanova, S.Vasyulya, P.Karalli; investigation, D.Glukhovets, A.Yushmanova, S.Vasyulya, P.Karalli.; data curation, S.Sheberstov; writing— D.Glukhovets, O.Kopelevich and others; writing—review and editing, O.Kopelevich; visualization, D.Glukhovets, A.Yushmanova, S.Vasyulya, P.Karalli, I.Sahling.

Funding: This research was supported by RFBR grant.19-55-45024.

Acknowledgments: The results were obtained in the framework of the state assignment of Minobrnauki RF (theme No.0149-2019-0003). We thank S.I. Pogosyan for a given opportunity to use the ICAM absorption meter in our expeditionary research; V.A. Artemiev, A.V. Grigoriev, A.N. Khrapko for their help in the field studies.

Acknowledgments: In this section you can acknowledge any support given which is not covered by the author contribution or funding sections. This may include administrative and technical support, or donations in kind (e.g., materials used for experiments).

Conflicts of Interest: The authors declare no conflict of interest. The funders had no role in the design of the study; in the collection, analyses, or interpretation of data; in the writing of the manuscript, or in the decision to publish the results”.

References

1. Perovich, D.K.; Nghiem, S.V.; Markus, T.; Schweiger, A.J. Seasonal evolution and interannual variability of the local solar energy absorbed by the Arctic sea ice–ocean system. *J. Geophys. Res.* **2007**, *112*(C3), C03005, doi:10.1029/2006JC003558.
2. Perovich, D. K.; Jones, K. F.; Light, B.; Eicken, H.; Markus, T.; Stroeve, J.; Lindsay, R. Solar partitioning in a changing Arctic sea-ice cover. *Ann. Glaciol.* **2011**, *52*, 192–196.
3. Kopelevich, O.V.; Sahling, I.V.; Vazyulya, S.V.; Glukhovets, D.I.; Sheberstov, S.V.; Burenkov, V.I.; Karalli, P.G.; Yushmanova, A.V. *Bio-Optical Characteristics of the Seas, Surrounding the Western Part of Russia, from Data of the Satellite Ocean Color Scanners of 1998–2017*; OOO «VASH FORMAT»: Moscow, Russia, 2018.
4. Kopelevich, O.V.; Sahling, I.V.; Vazyulya, S.V.; Glukhovets, D.I.; Sheberstov, S.V.; Burenkov, V.I.; Karalli, P.G.; Yushmanova, A.V. Electronic Atlas. Bio-Optical Characteristics of the Seas, Surrounding the Western Part of Russia, from Data of the Satellite Ocean Color Scanners of 1998–2018. Available online: <http://optics.ocean.ru/> (accessed on 31 July 2020).
5. Kopelevich, O.V., Sheberstov, S.V., Burenkov, V.I. et al. Assessment of underwater irradiance and absorption of solar radiation at water column from satellite data // Proc. SPIE, 2007, Vol. 6615, 661507
6. Amon, R.M.W. The role of dissolved organic matter for the organic carbon cycle in the Arctic Ocean. In *The Organic Carbon Cycle in the Arctic Ocean*, Stein, R., MacDonald, R. Eds.; Springer: Berlin, Germany, 2003; pp. 83–99, doi: 10.1007/978-3-642-18912-8_4.
7. Miller, W.L.; Moran, M.; Sheldon, W.M.; Zepp, R.G.; Opsahl, S. Determination of apparent quantum yield spectra for the formation of biologically labile photoproducts. *Limnology and Oceanography* **2002**, *47*(2), 343-352.
8. Pugach, S.P.; Pipko, I.I.; Shakhova, N.E.; Shirshin, E.A.; Perminova, I.V.; Gustafsson, Ö.; Bondur, V.G.; Ruban, A.S.; Semiletov, I.P. Dissolved organic matter and its optical characteristics in the Laptev and East Siberian seas: spatial distribution and interannual variability (2003–2011). *Ocean Science* **2018**, *14*(1), 87.
9. Matsuoka, A.; Ortega-Retuerta, E.; Bricaud, A.; Arrigo, K.R.; Babin, M. Characteristics of colored dissolved organic matter (CDOM) in the Western Arctic Ocean: relationships with microbial activities. *Deep Sea Research Part II: Topical Studies in Oceanography* **2015**, *118*, 44-52.
10. Gonçalves-Araujo, R.; Stedmon, C.A.; Heim, B.; Dubinenkov, I.; Kraberg, A.; Moiseev, D.; Bracher, A. From fresh to marine waters: characterization and fate of dissolved organic matter in the Lena River Delta region, Siberia. *Frontiers in Marine Science* **2015**, *2*, 108, doi:10.3389/fmars.2015.00108.
11. Matsuoka, A.; Boss, E.; Babin, M.; Karp-Boss, L.; Hafez, M.; Chekalyuk, A.; Proctor, C.W.; Werdell, P.J.; Bricaud, A. Pan-Arctic optical characteristics of colored dissolved organic matter: tracing dissolved organic carbon in changing Arctic waters using satellite ocean color data. *Remote Sens. Environ.* **2017**, *200*, 89–101, doi: 10.1016/j.rse.2017.08.009.
12. Fichot, C.G.; Kaiser, K.; Hooker, S.B.; Amon, R.M.W.; Babin, M.; Bélanger, S.; Walker, S.; Benner, R. Pan-Arctic distributions of continental runoff in the Arctic Ocean. *Sci. Rep.* **2013**, *3*, 1053, doi:10.1038/srep01053.
13. Matsuoka, A.; Bricaud, A.; Benner, R.; Para, J.; Sempéré, R.; Prieur, L.; Bélanger, S.; Babin, M. Tracing the transport of colored dissolved organic matter in water masses of the Southern Beaufort Sea: relationship with hydrographic characteristics. *Biogeosciences* **2012**, *9*(3), 925.
14. Brezonik, P.; Menken, K.D.; Bauer, M. Landsat-based remote sensing of lake water quality characteristics, including chlorophyll and colored dissolved organic matter (CDOM). *Lake and Reservoir Management* **2005**, *21*(4), 373-382.
15. Aiken, G.R.; Gilmour, C.C.; Krabbenhoft, D.P.; Orem, W. Dissolved organic matter in the Florida Everglades: implications for ecosystem restoration. *Critical Reviews in Environmental Science and Technology* **2011**, *41*(S1), 217-248.
16. Kothawala, D. Dissolved organic matter in inland waters and its impacts on drinking water quality. 2019.
17. Kuznetsova, O.A.; Kopelevich, O.V.; Sheberstov, S.V.; Burenkov, V.I.; Mosharov, S.A.; Demidov, A.B. Assessment of chlorophyll concentration in the Kara Sea based on the data of satellite scanner MODIS–AQUA. *Curr. Probl. Remote Sens. Earth Space* **2013**, *5*, 21-31.
18. Glukhovets, D.I.; Goldin, Y.A. Research of the relationship between salinity and yellow substance fluorescence in the Kara Sea. *Fundamentalnaya i Prikladnaya Gidrofizika* **2018**, *11*(3), 34–39, doi:10.7868/S2073667318030048.

19. Kubryakov, A.; Stanichny, S.; Zatsepin, A. River plume dynamics in the Kara Sea from altimetry-based lagrangian model, satellite salinity and chlorophyll data. *Remote Sensing of Environment* **2016**, *176*, 177-187, doi:10.1016/j.rse.2016.01.020.
20. Zavialov, P.O.; Izhitskiy, A.S.; Osadchiev, A.A.; Pelevin, V.V.; Grabovskiy, A.B. The structure of thermohaline and bio-optical fields in the surface layer of the Kara Sea in September 2011. *Oceanology* **2015**, *55* (4), 461-471, doi:10.1134/S0001437015040177.
21. Burenkov, V.I.; Goldin, Y.A.; Artem'ev, V.A.; Sheberstov, S.V. Optical characteristics of the Kara Sea derived from shipborne and satellite data. *Oceanology* **2010**, *50*(5), 675-687, doi:10.1134/S000143701005005X.
22. Lee, Z.; Carder, K.; Arnone, R. Deriving inherent optical properties from water color: A multiband quasi-analytical algorithm for optically deep waters. *Appl. Opt.* **2002**, *41*, 5755- 5772, doi: 10.1364/AO.41.005755.
23. Vazyulya, S.V.; Kopelevich, O.V.; Sheberstov, S.V.; Artemiev, V.A. Satellite estimation of the coefficients of CDOM absorption and diffuse attenuation in the White and Kara seas. *Curr. Probl. Remote Sens. Earth Space* **2014**, *11* (4), 31-41.
24. Pogosyan, S. I.; Durgaryan, A.M.; Konyukhov, I.V.; Chivkunova, O.B.; Merzlyak, M.N. Absorption spectroscopy of microalgae, cyanobacteria, and dissolved organic matter: Measurements in an integrating sphere cavity. *Oceanology* **2009**, *49*(6), 866-871.
25. Glukhovets, D.I.; Sheberstov, S.V.; Kopelevich, O.V.; Zaytseva, A.F.; Pogosyan, S.I. Measuring the sea water absorption factor using integrating sphere. *Light Eng.* **2018**, *26*, 120-126.
26. Pope, R.M.; Fry, E.S. Absorption spectrum (380-700 nm) of pure water. I. Integrating cavity measurements. *Appl. Opt.* **1997**, *36* (33), 8710-8723.
27. Yushmanova, A.V.; Kopelevich, O. V.; Vazyulya, S.V.; Sahling, I.V. Inter-annual variability of the seawater light absorption in surface layer of the northeastern Black Sea in connection with hydrometeorological factors. *J. Mar. Sci. Eng.* **2019**, *7*, 326, doi:10.3390/jmse7090326.
28. Artemiev, V. A.; Burenkov, V. I.; Vortman, M. I.; Grigoriev, A.V.; Kopelevich, O. V.; Khrapko A.N. Sea-truth measurements of ocean color: a new floating spectroradiometer and its metrology. *Oceanology* **2000**, *40*, 139-145.
29. Li, M.E.; Shibanov, E.B.; Martynov, O.V.; Korchemkina, E.N. Determination of the impurities concentration in the sea water on the range of the rising radiation brightness. *Morskoi gidrofizicheskii zhurnal* **2015**, *186*(6), 17-33.
30. Sheberstov, S.V. A system of batch processing of oceanological satellite data. *Curr. Probl. Remote Sens. Earth Space.* **2015**, *12*(6), 154-161.
31. Doerffer, R.; Schiller, H. The MERIS case 2 water algorithm. *International Journal of Remote Sensing* **2007**, *28*(3), 517-535.
32. Brockmann, C.; Doerffer, R.; Peters, M.; Stelzer, K.; Embacher, S.; Ruescas, A. Evolution of the C2RCC neural network for Sentinel 2 and 3 for the retrieval of ocean colour products in normal and extreme optically complex waters. In Proceeding of Living Planet Symposium, Prague, Czech Republic; 2016; ESA SP-740.
33. Werdell, P. J.; Franz, B.A.; Bailey, S.W.; Feldman, G.C.; Boss, E.; Brando, V.E.; Mangin, A. Generalized ocean color inversion model for retrieving marine inherent optical properties. *Applied Optics* **2013**, *52*(10), 2019-2037.
34. Werdell, P. J.; McKinna, L. I.W.; Boss, E.; Ackleson, S.G.; Craig, S.E.; Gregg, W.W.; Lee, Z.; Maritorena, S.; Roesler, C.S.; Rousseaux, C.S.; Stramski, D.; Sullivan, J.M.; Twardowski, M.S.; Tzortziou, M.; Zhang, X., An overview of approaches and challenges for retrieving marine inherent optical properties from ocean color remote sensing. *Progress in Oceanography* **2018**, *160*, 186-212.
35. Gordon, H. R.; Brown, O.B.; Evans, R.H.; Brown, J.W.; Smith, R.C.; Baker, K.S.; Clark, D.K. A semianalytical radiance model of ocean color. *J. Geophys. Res.* **1988**, *93*(D9), 10909-10924.
36. Lee, Z.; Carder, K. L.; Mobley, C. D.; Steward, R. G.; Patch, J. S. Hyperspectral remote sensing for shallow waters: 2. Deriving bottom depths and water properties by optimization. *Appl. Opt.* **1999**, *38*(18), 3831-3843.
37. Gordon, H. R.; Morel, A. Remote assessing of ocean color for interpretation of satellite visible imagery: A review. *Lecture Notes on Coastal and Estuarine Studies* **1983**, *4*, 44.
38. Smith, R.C.; Baker, K.S. Optical properties of the clearest natural waters, *Applied Optics* **1981**, *20*, 177 - 184.

39. Demidov, A.B.; Kopelevich, O.V.; Mosharov, S.A.; Sheberstov, S.V.; Vazyulya, S.V. Modelling Kara Sea phytoplankton primary production: Development and skill assessment of regional algorithms. *Journal of Sea Research* **2017**, *125*, 1-17.
40. Gordon, H.R. Can the Lambert-Beer law be applied to the diffuse attenuation coefficient of ocean water? *Limnol. Oceanogr.* **1989**, *34*, 1389–1409, doi:10.4319/lo.1989.34.8.1389.
41. Burenkov, V. I.; Ershova, S. V.; Kopelevich, O. V.; Sheberstov, S. V.; Shevchenko, V. P. An Estimate of the Distribution of Suspended Matter in the Barents Sea Waters on the Basis of the SeaWiFS Satellite Ocean Color Scanner. *Oceanology* **2001**, *41* (5), 622–628.
42. Glukhovets, D.I.; Goldin, Yu.A. Surface desalinated layer distribution in the Kara Sea determined by shipboard and satellite data. *Oceanologia.* **2020**, *62*, 364-373, doi:10.1016/j.oceano.2020.04.002.
43. Zatsepin, A.G.; Zavialov, P.O.; Kremenetskiy, V.V.; Poyarkov, S.G.; Soloviev, D.M. The upper desalinated layer in the Kara Sea. *Oceanology* **2010**, *50*(5), 657–667, doi:10.1134/S0001437010050036.
44. Lee, Z.-P.; Du, K.-P.; Arnone, R. A model for the diffuse attenuation coefficient of downwelling irradiance. *J. Geophys. Res.* **2005**, *110*, 02016, doi:10.1029/2004JC002275.
45. Kopelevich, O.; Sheberstov, S.; Vazyulya, S. Effect of a Coccolithophore Bloom on the Underwater Light Field and the Albedo of the Water Column. *J. Mar. Sci. Eng.* **2020**, *8*, 456. doi:10.3390/jmse8060456.
46. OLCI Level-2 Water WRR and WFR. Available online: <https://sentinel.esa.int/web/sentinel/user-guides/sentinel-3-olci> (accessed on 30 Aug 2020).